Fabry-Perot Sapphire Temperature Sensor for Use in Coal Gasification

Georgi Ivanov

Thesis submitted to the faculty of the

Virginia Polytechnic Institute and State University

In partial fulfillment of the requirements for the degree of

MASTER OF SCIENCE

IN

ELECTRICAL ENGINEERING

Anbo Wang, Chair

Gary R. Pickrell

Yong Xu

May 3, 2011

Blacksburg, VA

Keywords: Optical Fiber Sensors, Fourier Analysis, White-light Interferometry, Fabry-Perot

Fabry-Perot Sapphire Temperature Sensor for Use in Coal Gasification

Georgi Ivanov

ABSTRACT

Sapphire fiber based temperature sensors are exceptional in their ability to operate at temperatures above 1000°C and as high as 1800°C. Sapphire fiber technology is emerging and the fiber is available commercially. Sapphire fiber has a high loss, is highly multi-mode and does not have a solid cladding, but it is nonetheless very useful in high temperature applications. Of the available interferometer configurations, Fabry-Perot interferometers are distinguished in their high accuracy and great isolation from sources of error.

In this thesis, improvements are reported to an existing design to enhance its reliability and to reduce possible modes of failure. The existing high temperature sensor design has shown a lot of potential in the past by continuously measuring the temperature in a coal gasifier for 7 months, but its true potential has not yet been realized. The goal of this work and the work of many others is to extend the working life and reliability of high-temperature optical sapphire temperature sensors in harsh environments by exploring a solid cladding for sapphire fiber, improved fringe visibility sapphire wafers and a new sensor design. This project is supported by the National Energy and Technology Laboratory of the Department of Energy.

Acknowledgements

First of all, I would like to thank my advisor, Dr. Anbo Wang for his support and guidance throughout my graduate work. His intellect, professional talent and high caliber of character are not easily surpassed. It has been an absolute privilege to work for him for the past two years. I would also like to thank my committee members, Dr. Pickrell and Dr. Xu, for their assistance and support.

I would like to thank my project manager Dr. Evan Lally. His work ethic and keen insight have been a constant inspiration to me. I would also like to thank my second project manager Cheng Ma. His leadership has been valuable during the challenging period of sensor assembly.

I would like to thank Dr. Jiajun Wang for his training and patience during the early days of my studies.

In addition, I would like to thank my fellow lab members, Dorothy Wang, Bo Dong, Kathy Wang, Tyler Shillig, Michael Fraser, Guo Yu, Zhipeng Tian, Dr. Jianmin Gong, Brian Scott and Dr. Xiaoping Wang for their encouragement, help and friendship over the last two years. Many thanks go to Bo Dong for creating the custom new platen for wafer polishing.

I would like to thank my girlfriend Joy for all her love and support during my studies. She has inspired me in so many ways. In has been the greatest happiness to be with her since we first met at Virginia Tech. I would also like to thank my family for their care, guidance and encouragement.

Last but not least, I would like to thank the sponsor, the National Energy and Technology Laboratory (NETL) of the Department of Energy (DOE) for their support during my graduate study, which has allowed me to learn greatly and make contributions to the project.

Table of Contents

List of Figures

List of Tables

Chapter 1 Introduction

1.1 Introduction to Optical Sensors

Optical fiber was first demonstrated by Daniel Colladon and Jacques Babinet in Paris in 1842 by showing the light guiding properties of running water or a "light pipe."[1] In 1880, William Wheeler designed a system of glass tubes covered with a metallic layer and reflectors to light houses in Concord, Massachusetts[2]. His idea was to increase lighting efficiency by having a singular light source that can illuminate multiple lights. This idea did not catch on, but it might make a return in the form of solar lighting[3]. Since then, optical fiber has spawned many applications, including but not limited to: communication, power transfer and sensing. An optical fiber in its simplest sense is a cylindrical structure composed of two layers: core and cladding, see Figure 1.1.

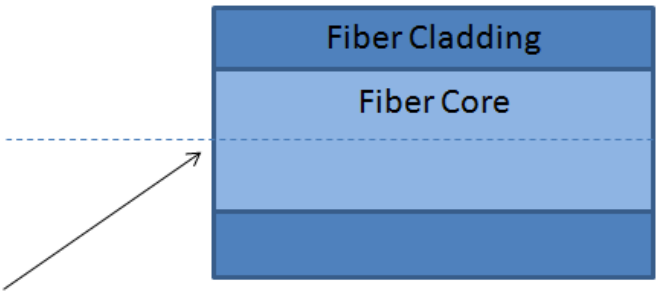

Figure 1.1 Simple generic optical fiber.

Since its inception the optical fiber has become a ubiquitous and highly developed part of society. Of its many uses, optical sensing is a developing field with many applications. One distinct advantage is fiber optic sensors and conduits are immune to electromagnetic interference (EMI)[4]. Different types of sensors include temperature, pressure, chemical, strain and many more. An optical fiber may be solely used to deliver optical signal, an extrinsic sensor, or it might also be used as the sensing element, an intrinsic sensor. From here on, the focus will be on extrinsic temperature sensors specifically.

1.2 Types of High-Temperature Temperature Sensors

1.2.1 Electrical Sensors

The strait forward approach to measuring a high temperature is through the use of a thermocouple. Thermocouples function based on the junction of two different metals based on the Seebeck effect. At the junction of two different metals, a voltage will be generated that depends on the composition of the metals and the temperature. The two different types of metals must be converted to the metal used inside the probe leads. At this junction, there is also a voltage generated that opposes the original voltage. If the original junction is placed in a hot region while the secondary probe junctions are place in a cooler region, the thermocouple system will generate a voltage proportional to the difference of the hot and cold temperatures[5]. This is the basis of a thermocouple. It is easy to use and cost effective.

1.2.2 Optical Sensors

Optical sensors at high-temperatures are divided into categories: amorphous and crystalline. Amorphous silica fibers are limited to temperatures lower than 1000^{o}C due to dopant diffusion, while crystalline fibers are not doped and are capable of operating at much higher temperatures. Sensors in these categories may be further limited by the use of other materials in the actual sensor and assembly. An additional limitation, beyond a high melting point, is a good coefficient of thermal expansion (CTE) match, not only at room temperature, but throughout the entire dynamic range of the sensor.

There are many possible designs for temperatures below 1000^{o}C due to a lower melting point requirement and a relaxed requirement on the CTE match enabling the use of many materials. A limitation is the availability of economical electric temperature sensors in this range that displace the need for optical sensors for the majority of applications. One interesting exception is the use of optical sensors for continuous temperature sensing. These designs are not the subject of this thesis.

There are limited optical sensor designs capable of operating above 1000^{o}C. A design by R. R. Dils in 1982 uses a blackbody cavity formed by a metallic layer at the tip of a sapphire single-crystal fiber to measure temperatures from 600^{o}C to 2000^{o}C with good accuracy, high

sensitivity and a rapid temporal response[6]. In 1999, this blackbody design was extended to temperatures as high as 2300C by the use of a zirconia single-crystal fiber by Tong *et al.*[7].

Another temperature measuring scheme relies on the temperature dependent lifetime of the fluorescent state in a phosphor as demonstrated by Kennedy and Djeu in 2002 by the fluorescence of Yb:YAG formed by dopping at the tip of a YAG fiber for temperatures up to 1600^{o}C[8]. This design shows no pressure or stress cross-sensitivity and can operate with minimal knowledge of the system. The temperate can be determined from the slope of the signal waveform alone without the knowledge of any other parameter.

A polarization-based design was demonstrated by Wang *et al.* to have a dynamic range of 25-1500^{o}C with a sensitivity of 5^{o}C[9]. This sensor included birefringence balancing by aligning two 37.9mm sapphire rods end-to-end fast-axis to slow-axis. The temperature is determined from the dramatic change in relative intensity.

Various temperature sensing designs based on a Fabry-Perot (FP) interferometer have been demonstrated by Wang *el al*. The first is an Intrinsic Fabry-Parot Interferometer (IFPI) design on a single-mode silica fiber by the reflections from the splice point to a 32mm multi-mode sapphire fiber and the far polished end of the sapphire fiber[10]. The dynamic range demonstrated is 310-976^{o}C with a resolution of 0.2^{o}C. Later, the dynamic range was expanded to 256-1510^{o}C with a temperature resolution of only 0.1^{o}C by heating only 5mm out of a 31mm sapphire fiber with an oxygen-propane torch[11].

Extrinsic Fabry-Parot Interferometer (EFPI) configurations include an interferometer between the tip of a sapphire fiber and a metallic surface, and an interferometer between the tip of the lead-in sapphire fiber(R2) and the tip of another sapphire fiber(R3) at distance[12][13], shown in Figure 1.2. This sensing method laid down the foundation for the method used in this project, described in the following section.

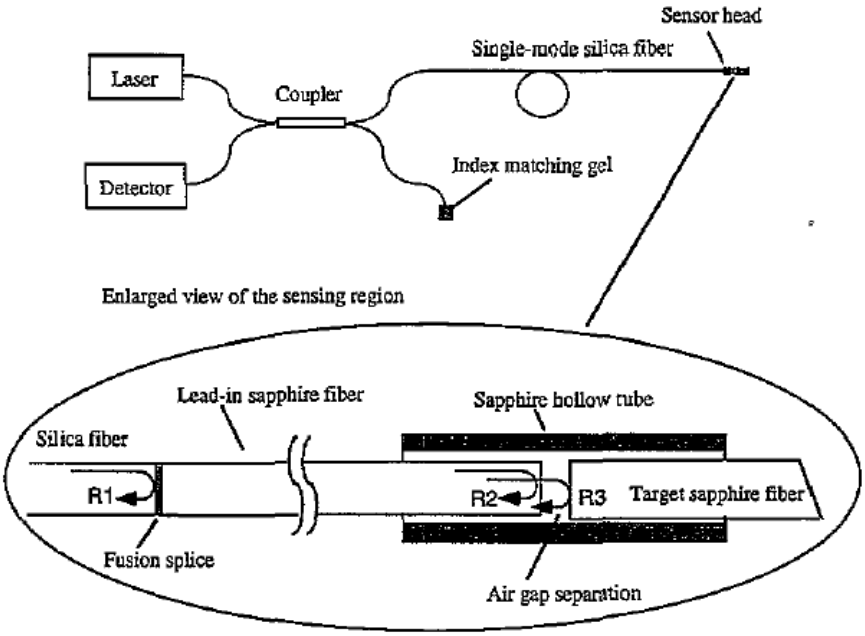

Figure 1.2. EFPI air-gap sapphire fiber sensor.[13]

1.3 Sensing Method

In this project, the required temperature range is 25-1600°C, making the use of silica in and around the sensor infeasible. Note however, that silica may still be used in lower temperature regions and leading to the interrogation system.

An increase in temperature corresponds to an expansion in most solid materials, which is measured by the coefficient of thermal expansion (CTE). CTE's for many materials has been studied and well documented. Data from several sources have been combined to form the CTE versus temperature curve for sapphire shown in Figure 1.3. Note that the CTE of sapphire is always positive and only varies slightly with temperature, which translates to a consistent change in thickness and sensor sensitivity. The sensor works by optically measuring the thickness of a sapphire wafer using a Fabry-Perot interferometer precisely enough to detect changes in thickness resulting from a small change in temperature.

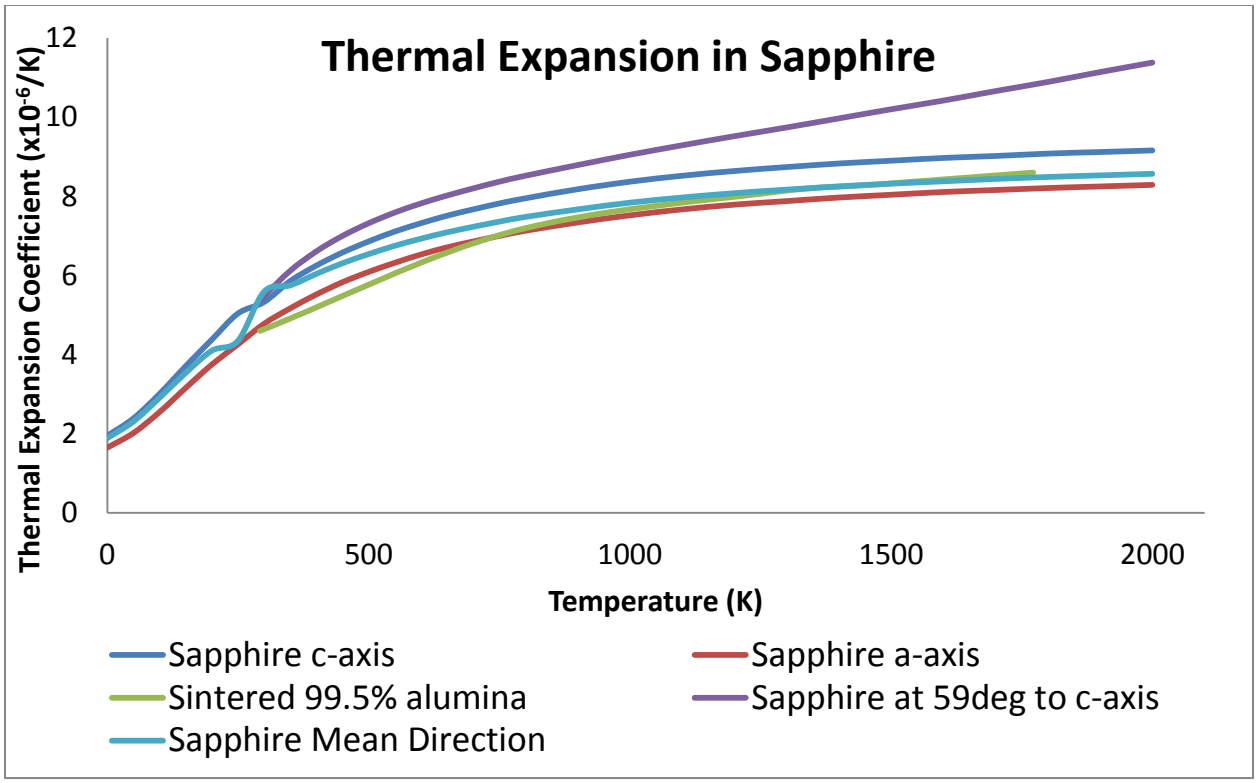

Figure 1.3. Thermal Expansion in Sapphire and Alumina in terms of CTE.

1.4 Organization of Thesis

Chapter 2 covers the operation and design parameters of the Fabry-Perot interferometer. Chapter 3 explores signal processing means for measuring wafer thickness and parallelism. Chapter 4 recaps work done to create a solid cladding for sapphire fiber. Chapter 5 details the work done to produce wafers of sufficient quality to meet the requirements of the project. Chapter 6 discusses the new generation sensor probe, as well as comparing it the previous design. Finally, Chapter 7 summarizes the progress made and outlines possible future improvements.

Chapter 2 Sensor Principle and Measurement Scheme

2.1 Fabry-Perot Interferometer Theory

The Fabry-Perot Interferometer is only one example of the broader family of interferometers. An interferometer superimposes electromagnetic waves to generate an interference pattern. When two optical beams co-propagate with the same velocity, or mode, they are said to have interfered and are no longer optically separable. The Fabry-Perot Interferometer functions by the use of two partially reflective surfaces placed close together, see Figure 2.1[14].

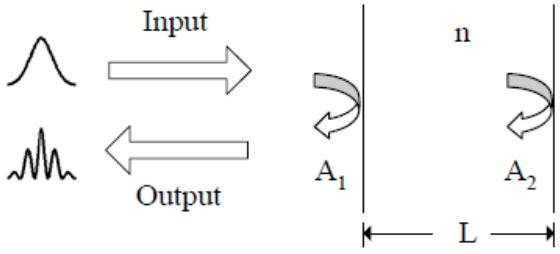

Figure 2.1. Fabry-Perot Interferometer[27].

After two coherent beams of the same frequency have interfered, the result depends on the relative phase. From Figure 2.1, it is clear that beam A_2 will travel a longer distance than beam A_1, when the beams interfere at the reflection point of A_1. The difference in distance is equal to 2*L in a material with an index of reflection n. To remove the dependence on material, the optical path difference is defined as 2*n*L in a free-space virtual material with velocity c (the speed of light), Equation 2-1. Either way, the time delay is the same, see Equation 2-2.

$$OPD = 2 * n * L \tag{2-1}$$

$$\Delta t = \frac{2*L}{v} = \frac{2*L}{c/n} = \frac{2*n*L}{c} = \frac{OPD}{c} \tag{2-2}$$

Since the two beams are periodic with the same frequency, a way to measure the relative phase is to look at how many extra wavelengths have been traveled or OPD/λ. The full cycles traveled are of no consequence to relative phase and thus of no interest, but partial

cycles crease a phase mismatch. This is compared to the reflection at A_1 which undergoes a half cycle phase shift upon a normal incidence reflection due to an increase in refractive index. If the relative additional fraction of a cycle is 0, there will be a perfect match of the interfering beams or constructive interference. On the flip side, if the extra distance traveled results in a half-wavelength remainder, there will be perfect mismatch or destructive interference. If one cycle is scaled to 2π, then constructive interference is at 0 and destructive interference is at π. The resulting optical beam will have a power that is maximal at constructive interference and minimal at destructive interference. This oscillatory behavior with a scaling factor of 1 is embodied in the complex exponential function as the electric field amplitude A_2 oscillates around A_1. The equation described so far is squared to convert to intensity and shown in Equation 2-3. The complex exponential becomes $\cos(2\pi*\mathrm{OPD}/\lambda)$ and contains the useful information in a much larger collection of signals received by the spectral power measuring spectrometer. If the cavity length (L) changes, so will the interference pattern at any single wavelength.

$$I(\lambda) \propto \left| A_1 * e^{-j\pi} + A_2 * e^{-j*2\pi*\frac{\mathrm{OPD}}{\lambda}} \right|^2 = A_1^2 + A_2^2 - 2A_1A_2 \cos\left(\frac{2\pi*OPD}{\lambda} + \varphi_0\right) \quad (2\text{-}3)$$

2.2 White Light Interferometry

The useful part about the previously described interferometer is that an interference pattern forms for each wavelength, at the same time. At any given cavity length, there will be many wavelengths are experiencing constructive interference, see Figure 2.2 and Equation 2-4, and many wavelengths experiencing destructive interference, while the majority are in between.

$$OPD = \lambda * m \quad (2\text{-}4)$$

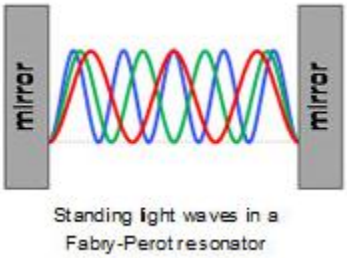

Figure 2.2. Multiple Wavelengths of Light Constructively Interfering[28].

Clearly, dividing the OPD by any integer number (m) of wavelength iterations will yield a wavelength that interferes in the interferometer. This is simply the reverse of the relationship between λ and OPD described in the previous section. Notice that increasing m yields smaller and more frequent λ. This means the intensity peak locations are not linear with wavelength. If the interferometer is powered equally at all wavelengths between 0 and OPD and the reflected power spectrum measured, the waveform (fringes) will decrease in frequency with the increasing wavelength axis, shown in Figure 2.3.

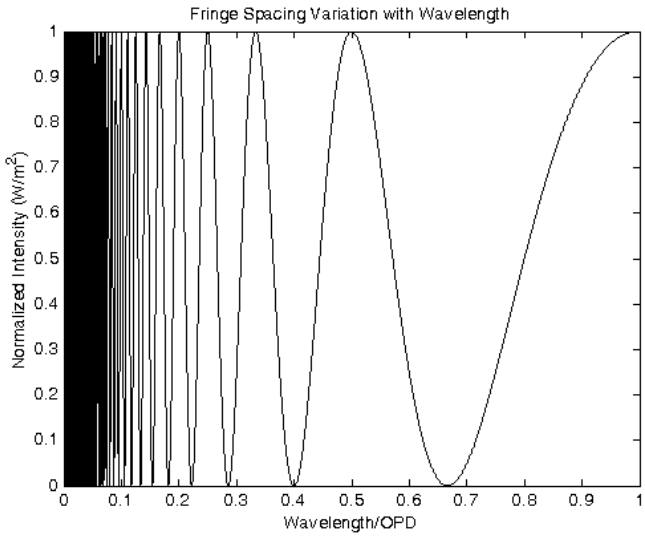

Figure 2.3. Fringe Frequency Decreases with Wavelength

The actual peak locations and fringe frequency are dependent on the OPD. In choosing the illumination source wavelength range, the spectrometer wavelength range and resolution for measuring OPD, one must be conscious of the desired range of cavity lengths to be measured. The greater the number of peaks, the more accurate the measurement that can be

made; but too many peaks and there will be too few samples per wavelength. Signal processing will be discussed in Section 2.4.

In the ideal case discussed so far everything that can interfere will, but in real life that is not always the case. Lasers have a quoted coherence length value. This number represents the distance over which the laser will on average output a constant phase signal. It is defined as the OPD in a self-interfering Michelson interferometer corresponding to a fringe visibility (FV) of 37%. FV is defined in Equation 3-1, where 1 is an ideal signal and 0 is no signal. The OPD must be well under the coherence length for clear fringes to be seen. There are a number of other factors diminishing FV, including reflecting surface imperfections in the Fabry-Perot cavity, additional reflections, light source spectral intensity profile, photo-detector statistical errors and black-body radiation.

2.3 Introduction to the System Setup

The goal of the project is to accurately measure the cavity length as it changes with temperature. In order to measure the cavity length of the sensor, an input light beam must be generated and the reflected signal analyzed, see Figure 2.4. The Fabry-Perot Interferometer is a sapphire wafer with a thickness in the range of 10-100μm. It is fixed in place by an alumina tube and connected using a high-temperature alumina adhesive, Contronics Resbond 903HP. Light is guided to and from the wafer by a 50cm sapphire fiber inserted into the alumina tube and fixed using the alumina adhesive. The sapphire fiber is connected to a silica fiber by a thermal fusion technique based on a lower silica core melting point than the cladding[17]. A 2x2 50:50 multimode coupler connects the silica fiber to the 850nm LED light source and the OceanOptics spectrometer. The unused coupler end is immersed in an index-matching gel to reduce the reflection from the end of the fiber.

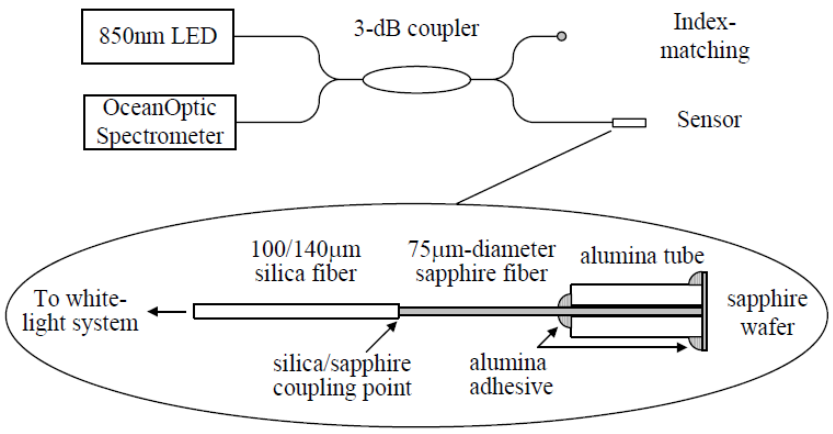

Figure 2.4. Complete System Schematic[27].

2.4 Introduction to the Signal Processing

The full model describing the system in Figure 2.4 is shown in Equation 2-5[22]. The r's are reflectance values, where r_{A1} and r_{A2} represent the Fabry-Perot interferometer in Equation 2-3, r_{splice} is the reflection from the sapphire-to-silica splice and r_{end} is the reflection from the end of the sapphire fiber. Since these are reflections, they are all magnitude dependent on the intensity of the light source. The other sources of light are blackbody radiation (I_B) which is a function of temperature and dark current (I_D) from the statistical error in the photo-detector.

$$I_{total}(\lambda) = I_B(\lambda) + I_D(\lambda) + I_{source}(\lambda)\left[r_{splice} + r_{end} + r_{A1} + r_{A2} - 2V\sqrt{r_{A1}r_{A2}}cos\frac{2\pi * OPD}{\lambda}\right] \quad (2\text{-}5)$$

The OPD from which the temperature can be extracted is only contained in the cos(2π*OPD/λ) term. There are many ways to extract the OPD information from the above expression. The quickest and easiest is to take any two adjacent peaks and find the wavelength they occurred at. From Equation 2-4, two adjacent peaks would have consecutive integer fringe number values, Equation 2-6. Some further calculation yields Equation 2-7. This equation, although quick and effective, is only based on two points from a spectrum composed of hundreds of points. More sophisticated schemes for extracting the OPD from a spectrum will be covered in Chapter 3.

$$\frac{OPD}{\lambda_1} = m \qquad \text{and} \qquad \frac{OPD}{\lambda_2} = m\text{-}1 \quad (2\text{-}6)$$

$$\frac{OPD}{\lambda_1} - \frac{OPD}{\lambda_2} = 1 \implies OPD = \frac{\lambda_2 \lambda_1}{\lambda_{2-} \lambda_1} \tag{2-7}$$

An estimate of the error in Equation 2-8 can be obtained by differentiation[19].

$$\Delta OPD = \left[\frac{\lambda_2}{\lambda_2 - \lambda_1} + \frac{\lambda_1 \lambda_2}{(\lambda_2 - \lambda_1)^2}\right]\Delta\lambda_1 + \left[\frac{\lambda_1}{\lambda_2 - \lambda_1} - \frac{\lambda_1 \lambda_2}{(\lambda_2 - \lambda_1)^2}\right]\Delta\lambda_2 = \frac{{\lambda_2}^2 \Delta\lambda_1 - {\lambda_1}^2 \Delta\lambda_2}{(\lambda_2 - \lambda_1)^2}$$

$$\Delta OPD = \left[\frac{\lambda_1 \lambda_2}{(\lambda_2 - \lambda_1)^2}\right]\left(\frac{\lambda_1}{\lambda_2}\Delta\lambda_1 - \frac{\lambda_2}{\lambda_1}\Delta\lambda_2\right) = \frac{OPD}{\lambda_2 - \lambda_1}\left(\frac{\lambda_1}{\lambda_2}\Delta\lambda_1 - \frac{\lambda_2}{\lambda_1}\Delta\lambda_2\right)$$

$$\frac{\Delta OPD}{OPD} = \frac{1}{\lambda_2 - \lambda_1}\left(\frac{\lambda_1}{\lambda_2}\Delta\lambda_1 - \frac{\lambda_2}{\lambda_1}\Delta\lambda_2\right)$$

$$\frac{\Delta OPD}{OPD} = \frac{\Delta\lambda_1 - \Delta\lambda_2}{\lambda_2 - \lambda_1} \tag{2-8}$$

Once an accurate value for OPD is obtained, it can be immediately converted to L, the cavity length, by Equation 2-1. As covered in Section 1.3, L changes predictably with temperature. A theoretical value for the cavity length can be calculated for each temperature. However, if there is any deviation from the model, there would be an error in the temperature calculation. Instead experimental results taken from the real sensor are more accurate. Experimental OPD measurements are recorded at temperatures throughout the dynamic range. A temperature calibration curve is created by drawing a continuous fitted curve across the discrete calibration points. There is no need to convert to L as it is only a function of OPD.

Chapter 3 Wafer and Sensor Measurement Scheme

3.1 Evaluation of Sensor Performance

In order to classify how well a sensor's signal can be seen, it is necessary to define a signal-to-noise ratio standard. Signal-to-noise ratio is defined by the average signal power divided by average noise power. The power in the temperature sensor system varies with wavelength. Figure 3.1 depicts the intensity versus wavelength relationship for the LED source. It is clear the intensity is the highest at the 850nm wavelength and fades in both directions. The system is the most sensitive at 850nm, because it is the wavelength where the light source intensity is the greatest. The dark current and blackbody radiation are independent of the light source. A signal-to-noise ratio calculated at 850nm, instead of the whole spectrum, is more indicative of the best visibility seen. This ratio is called the fringe visibility[20].

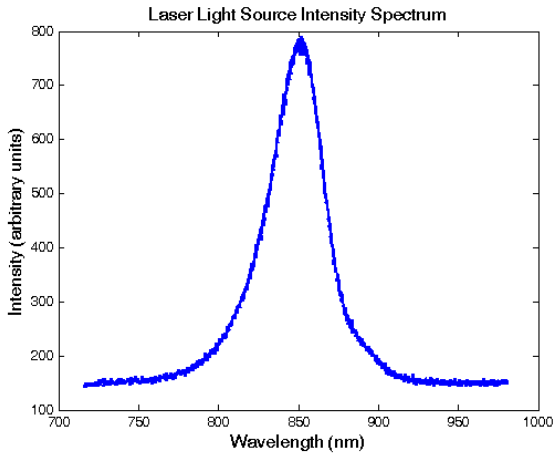

Figure 3.1. Light source laser intensity spectrum.

Fringe visibility seeks to quantify the effect of unwanted DC (zero frequency) components, while zero-mean errors, like dark current, are ignored. This is useful because black-body radiation is a noise with a large DC component that increases with temperature. Noise (not modeled) from the black-body radiation and the photodiode statistical error can swamp the signal if fringe visibility is low. Fringe visibility is modeled as a sinusoid with an added DC component. In this case, the amplitude of the sinusoid is $(I_{max}-I_{min})/2$ and magnitude of the background is (Imax+Imin)/2, centered around 850nm. Both the I_{max} and I_{min} values should be ideally taken at 850nm, where they are both at maximum. A simple approximation is

to take the closest I_{max} and I_{min} to the 850nm wavelength. A more sophisticated approach is to use the Hilbert transform to get the bounding envelope of the spectrum, see Figure 3.2[20]. The formula for fringe visibility is shown in Equation 3-1. A fringe visibility of 1 is ideal and a fringe visibility of 0 means the signal has been lost.

$$FV = \frac{amplitude\ of\ sinusoid}{average\ DC\ component} = \frac{\frac{I_{max}-I_{min}}{2}}{\frac{I_{max}+I_{min}}{2}} = \frac{I_{max}-I_{min}}{I_{max}+I_{min}} \tag{3-1}$$

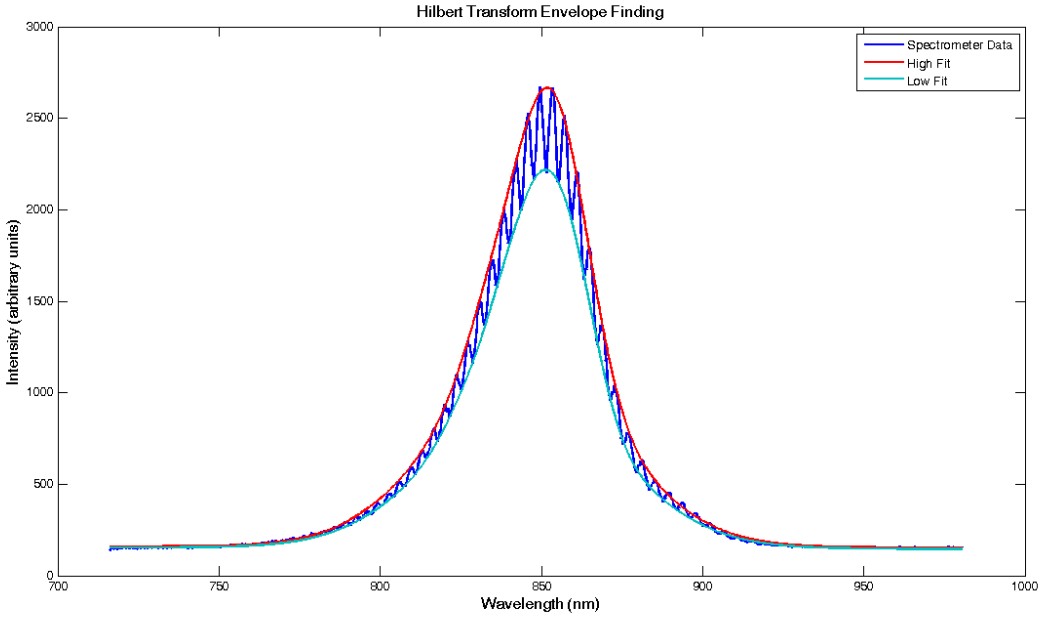

Figure 3.2. Hilbert Transform Envelope Finding FV calculation.

A fringe visibility of 1 is ideal, but in a low-finesse sensor using sapphire fiber, it is not seen. Low-finesse means a small reflection coefficient in the interferometer. For a sapphire-to-air interface, the reflectance is 7.6% by the Fresnel equations at normal incidence calculated in Equation 3-2. The interferometer returns only a small fraction of the incident intensity. Immediately next to the interferometer is a sapphire-to-air reflection from the end of the sapphire fiber. This reflection at best only adds to the DC component, but considering it is touching the wafer, the reflection can interfere with the Fabry-Perot interferometer, creating a second cavity length and skewing the OPD data. Fortunately, interference can be avoided by polishing the end-face of the sapphire fiber 1^{o} from perpendicular.

$$R = \left(\frac{1\cos(O)-1.76\cos(0)}{1\cos(0)+1.76\cos(0)}\right)^2 = 0.0758 \tag{3-2}$$

The next obstacle is the large about 0.3dB/cm intensity loss from the sapphire fiber[22]. The incident light travels 50cm through the interferometer, where 7-14% of the light is reflected back. Then the light travels 50cm back through the sapphire fiber. The round trip loss from the sapphire fiber is about 30dB. There are additional coupling losses from the silica-to-sapphire splice both in the forward and reverse directions. The silica-to-sapphire splice has a reflectance of 0.44% by the Fresnel equations at normal incidence. This may be much smaller than the 7.6% sapphire-to-air reflection, but the 7.6% reflection has gone through a 30dB intensity loss and not quantified coupling loss. From sapphire fiber loss alone, the 7.6% intensity reflection goes down to 7.6×10^{-3}%. At this point, it is critical to minimize any noise or other reflections. The silica-to-sapphire splice point reflection can be minimized by polishing the sapphire fiber at an angle and by applying an antireflective coating. Both methods are under exploration at the CPT, pursued by Guo Yu[18]. Additional, 3dB losses are incurred twice from the 50:50 coupler: once in the forward direction and once in the reverse direction. This can be minimized by using a multimode circulator instead of a coupler, but this is not a priority since there are no reflections after the coupler. The photodiode inside the spectrometer does receive a very weak signal that is vulnerable to even small amounts of noise. On the flipside, instead of maximizing the percentage of returned power, opting for a more powerful LED light source could achieve the same effect, see Equation 2-5. The advantage is blackbody radiation, a major source of noise, will remain unchanged, while the interference signal, proportional to the LED intensity, will increase.

The Fabry-Perot interferometer is formed by a sapphire wafer. From the outline of losses and undesirable reflections in the previous paragraph, it is clear that the wafer needs to produce the highest reflections possible. These are produced by a perfect wafer with no defects. Once the light leaves the wafer, it is all cumulative losses from there. Factors related to the functionality of a wafer are wafer thickness, wafer face flatness, wafer face smoothness and wafer parallelism.

Light coming from the LED diode has an unknown but small, on the order of tens of micrometers, coherence length. A smaller cavity length means a smaller total phase delay,

which would result in more light interfering. For this project, it is desirable to have a wafer that is as thin as is possible to manufacture, as long as the wafer is strong enough be handled.

It is desirable that the wafer area used has a constant thickness and consistent fringe visibility. If the sapphire fiber that reads the fiber shifts inside the tube and moves up to 100μm in any direction, the temperature reading should not change by much. The wafer can't be perfectly flat but the change in thickness should be minimal.

Since the central interrogating wavelength is 850nm, imperfections in the wafer surface should be much smaller than 850nm. Any features on the same order of magnitude as 850nm will cause scattering, see Figure 3.3. It is extremely important that the wafers are polished to a smooth finish, on the order of 100nm or better.

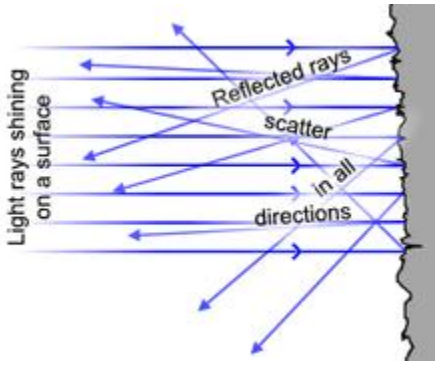

Figure 3.3. Illustration of scattering[29].

The last requirement on the quality of the sapphire wafer is parallelism between the front and back surfaces of the wafer. If the two surfaces are assumed to be planar, a wedge angle can be defined in the direction of maximum angle.

3.2 Evaluation of Wafer Thickness

3.2.1 Time-domain Methods

Although it is the equivalent of the time-domain, the label on the axis is wavelength. As discussed in Section 2.2, the spectrum peaks are not linear with wavelength but with one divided by wavelength. By making the substitution in Equation 3-3, Equation 2-5 becomes Equation 3-4. For physically sampled data, regularly spaced samples in the t scale(often also referred to as the k scale) can be obtained by linear interpolation.

$$t = \frac{1}{\lambda} \tag{3-3}$$

$$I_{total}(\lambda) = I_B\left(\frac{1}{t}\right) + I_D\left(\frac{1}{t}\right) + I_{source}(\frac{1}{t})\left[r_{splice} + r_{end} + r_{A1} + r_{A2} - 2V\sqrt{r_{A1}r_{A2}}cos(2\pi * OPD * t + \varphi_0)\right] \tag{3-4}$$

All functions of t in Equation 3-4 and slow varying, except for $\cos(2\pi * OPD * t + \varphi_0)$. This is now a regular cosine in terms of t. The desired information, OPD, is extracted as precisely as possible. Accuracy is not important here; repeatability is. It is alright if the OPD obtained does not reflect the physical thickness, as long as there is enough precision and repeatability to track changes due to thermal expansion.

3.2.1.1 Sine-fit

A simple way to obtain the OPD of the sinusoid signal in the waveform is to use regression to fit a pure cosine to the graph. Before that is done, the graph need to be cleaned up by either normalization or frequency-domain filtering to remove all components other than the cosine. Once the cosine is fitted, the OPD can be immediately calculated by comparison to Equation 3-4[19].

3.2.1.2 Fabin's Method

Another method involves finding the period of the previous sinusoid by simple linear regression. Staring with points in the t scale, all of the points where the curve is positive are grouped together and weighted-averaged around each peak to find the centroid. These are the peaks of the sinusoid that was fitted in Section 3.2.1. Instead, simple linear regression is used to fit a straight line through the points offset by phase by the principle of phase unwrapping[31]. A second regression is done on the error to term to compensate. The difference is this method takes into account absolute peak locations, which are also related to the OPD.

3.2.2 Frequency-domain Method

One interesting detail about both of the previously mentioned time-domain methods is that they both used frequency-domain filters. So to find the period of the signal the time-domain functions, first it is found in the frequency-domain and then a very narrow filter is applied to separate it. Only to, then use the time-domain signal and some form of regression to find an estimate for the period.

Frequency-domain analysis and filtering are necessary for the time-domain methods, but instead of converting back to a time-domain signal, it is possible to obtain an estimate for OPD in the frequency-domain. By definition, period is one divided by frequency. By finding the exact location of the peak, OPD can be directly obtained from the frequency. Actually, the OPD is equivalent to the frequency. By comparison of cos(wt), where w is 2*pi*f and t is time in the time-domain equivalent, to Equation 3-4, it is visible that the OPD and the frequency are synonymous.

The limitation of the discrete Fourier transform is a finite number of samples. To get an infinitely accurate result for frequency, an infinite number of samples are required[21]. This is why the time-domain methods are popular. They first isolate the frequency in the frequency-domain, and then find it through regression in the time-domain. In this way, a better approximation for the frequency can be obtained with minimal effort.

The frequency-domain is far more powerful for analyzing frequency than the time-domain. Let's look at an example. If the right precautions aren't taken, the end of the fiber will interfere with the wafer. Since the fiber is touching the wafer, the OPD value of the new second interferometer is roughly the same as the value of the original interferometer. Nonetheless, the two OPD's, and thus frequencies, are not the same. Observe that in Figure 3.4 there are two peaks. Only one of them is the signal. Also, observe a peak with a high intensity to the far left. This peak is attributed to the DC component and it can throw off automatic peak detection. An easy way to exclude DC component noise is by using the expected value of the OPD to create a range for observation. Back to the two peaks in the middle of the figure, an assumption can be made that the slightly stronger peak corresponds to the desired wafer interferometer. If a time-domain method comes through and filters around the maximum peak as well as some of the trailing edges, both peaks will be captured. In the time-domain, the two peaks are indistinguishable and the regression results will be in between the two frequencies. The output will be an average of the two OPDs and the user will be none the wiser. This is acceptable though, for as long as the second interferometer remains unchanged. As soon as the fiber shifts, there will be an error introduced into the temperature reading. The fiber changing position with

respect to the wafer is undesirable in any case, because no wafer is perfect and the fiber will start reading the average thickness of a new location that likely has a different average thickness. Another way to sort of the peak ambiguity is by assuming the peak is from interference with the sapphire fiber tip. The sapphire fiber interferometer will have a larger OPD than the original wafer, which translates to a larger frequency. Under this assumption, the desired peak will always be the lower frequency one.

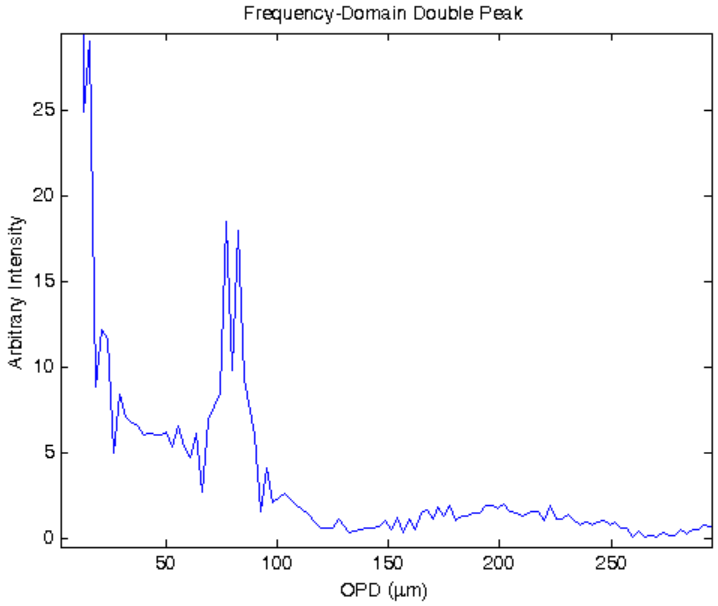

Figure 3.4. Visible Frequency Double-Peak and an Even Larger Low Frequency Peak.

Now to find the OPD in the frequency-domain, there is still the issue of the small sample set. One standard way of minimizing the effect of the discontinuity the ends of the sample set is through the use of a windowing function. The sinusoidal signal should be able to tessellate in the time-domain, to add up to the right frequency in the frequency domain. A windowing function has smooth tails that trail off to a small value at both ends, see Figure 3.5. When the time domain signal is multiplies by the window function, the frequency domain experiences a convolution. As a result each new frequency point depends on its neighbors. This can offset the frequency peak location, but it effectively reduces noise from non-tessellating time-domain signals. Windowing is clearly not good for a frequency-domain OPD determination. A filter design must have a flat region in the frequency area of interest. One example of such a filter is a finite impulse response (FIR) band-pass filter.

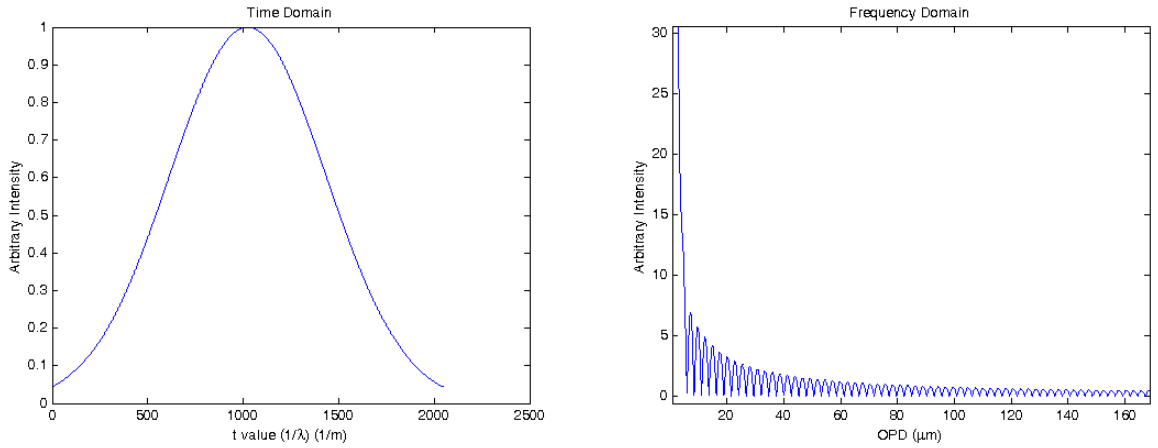

Figure 3.5. Gaussian Window Function in Time(left) and Frequency(right) Domains.

Zero-padding can be use to achieve more points in the frequency domain, however all points based the limited time-domain sample set. No matter how many points are added, the frequency resolution will remain the same, as frequency resolution is a function of the sampling rate(the spectrometer resolution). Zero-padding is inefficient when a large number of points like 1 trillion are used. Ten times more points must be used for each extra significant digit. However, the area of interest is much smaller that the whole fft graph. There is no point is computing 1 trillion values, if only 100 noncontiguous values will be used. Instead a function was created to compute the fft at specified frequency values and only at those points, see Appendix B. This gives unlimited precision in the frequency-domain quickly and efficiently. However this is nothing new, as the Fourier transform by definition is continuous. The accuracy of the transform however has not changed and it is still limited by the finite number of time-domain points and the sampling rate.

A finite set of data is equivalent to the infinite set of data with a time-domain rectangular window function applied to it. This is realized by zero padding. The second continuous treatment in the second method effectively puts the zeros between integer values but it never evaluates them. The sample still has to tessellate in the time domain. However, the cutoff at the ends of the time-domain sample is at random locations. When two samples are place side-by-side, there is a phase discontinuity in the desired frequency sinusoid. An attempt was made to eliminate this phase discontinuity by clipping the time domain sample at multiple points. Statistically, some sub-ranges in the time-domain sample set will have a smaller phase

mismatch then others. Collecting a large number of sub-ranges should create a distribution of phase mismatches. This distribution is still unidentified and very sensitive to noise.

As an example of clipping, up to 100 points were removed from the beginning of the sample set and up to 100 points were removed from the end of the sample set, in every possible combination for a total of 10,000 points, see Figure 3.6. A 3 dimensional version is shown in Figure 3.7, where the x and y axes represent clipping individual data point from the beginning and the end of the time-domain data set, respectively. Figure 3.6 is similar to an X-Z view of Figure 3.7. There is a pattern created and its DC value is a better approximation for OPD value. One easy way to approximate the OPD value is by averaging. The OPD value can be extracted from a subset of this pattern with a high accuracy and precision, however this method is infuriatingly slow. The more accurate the approximation for OPD, the larger number of frequency peaks that needs to be computed in the pattern. Each point requires a separate continuous Fourier transform approximation of the peak location. Using this method, 10 significant figures of accuracy have been achieved on a simulated ideal noise-free sinusoid. This method still needs some work. Filtering may be necessary to clean up the signal. The expected curve, a sinusoid in both directions, is shown in Figure 3.8 left. This is not what is observed in Figure 3.7 or Figure 3.8 right.

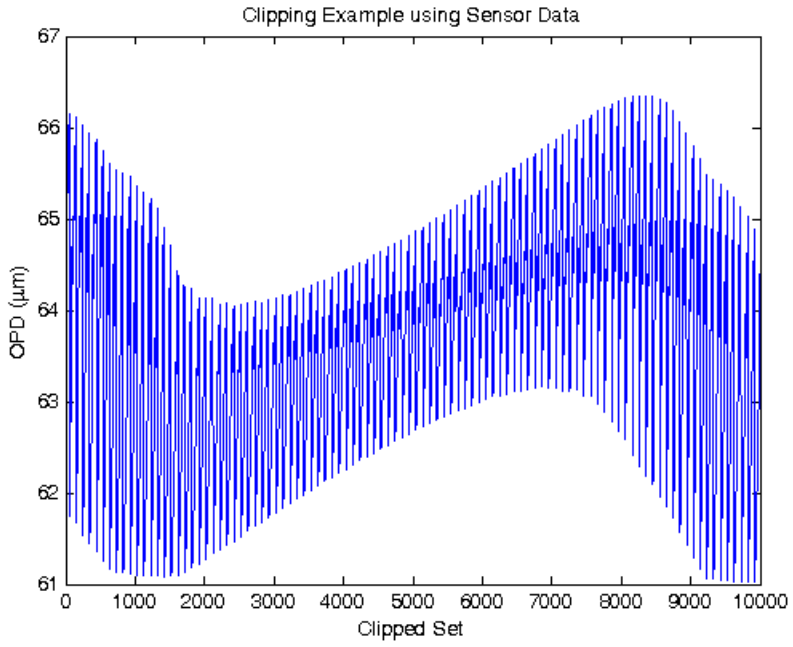

Figure 3.6. Example of point clipping.

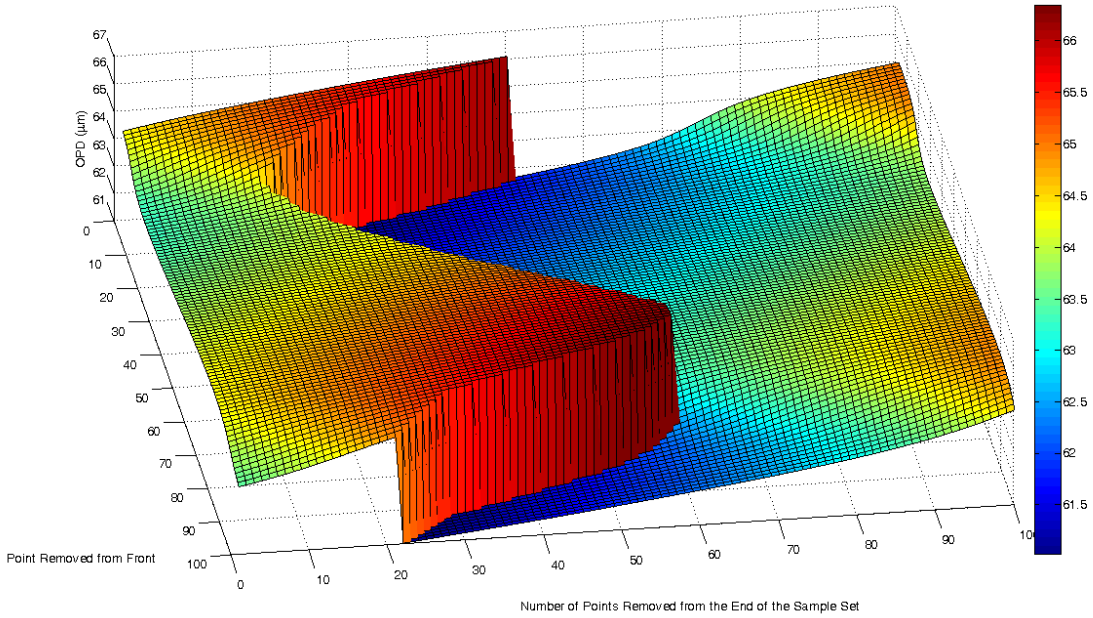

Figure 3.7. Example of point clipping in 3 dimensions.

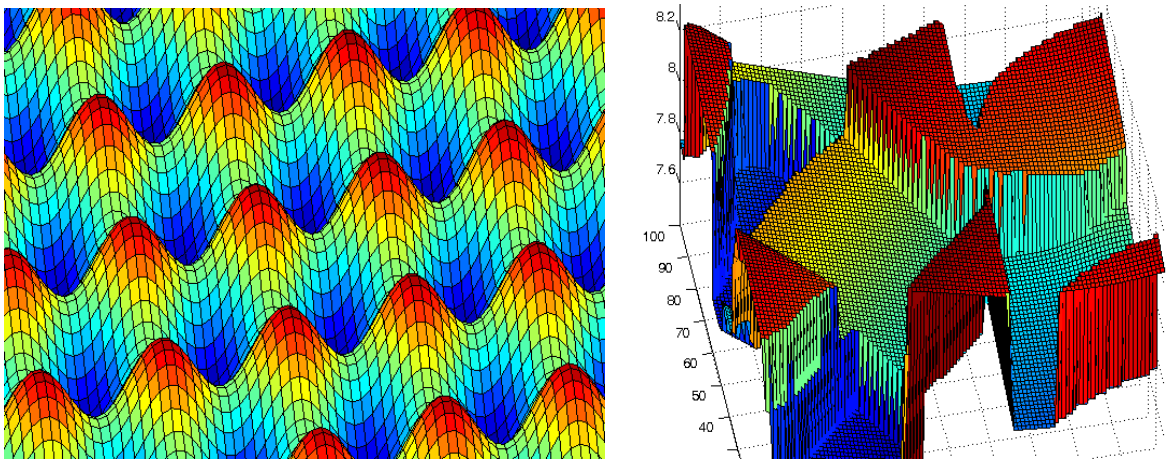

Figure 3.8. Left, ideal pattern that is sinusoidal. Right, random defects with high black-body radiation noise.

3.3 Evaluation of Wafer Wedge Angle

As discussed in Section 3.1, the sapphire wafer relevant characteristics are wafer thickness, surface roughness, surface contours and a wedge angle. Measurement of wafer thickness, the temperature sensing dimension, was discussed in Section 3.2. Surface roughness is hard to measure fiber-optically, but can be observed with a powerful microscope. A lack of surface quality would cause a decrease in the coherent reflections of the interferometer and ,

thus causing decrease in the fringe visibility. Surface roughness is a function of the polishing process, where it can be controlled. It will not be measured here. The two remaining aspects are surface contours and wedge angle.

3.3.1 Planar Approximation of Wedge Angle by Sampling at Multiple Points

Wedge angle is a function of the surface contours and is constantly varying with surface position. When classifying wafers, it is useful to come have only one number per wafer. This was done by assuming both of the wafer surfaces are planar. This is actually quite common with professionally polished wafers, where a large disk with a radial pattern is diced to yield smaller locally planar wafers. When both surfaces are planar, there is only one angle where the two planes intersect.

In Figure 3.9, the wafer has its bottom plane in the x-y plane at z=0. The thickness of the wafer is in the positive z direction with a slanted top plane. The procedure is to take OPD readings at opposite corners of a square region on the wafer and connect them with a vector. The vectors are each defined with a displacement d in the x-y plane equal to the diagonal of the square region, and a displacement Δz in the z direction equal to the difference in wafer thickness between the end and the beginning of the vector, see Equations 3-5 and 3-6. The cross product of the two vectors gives a normal vector to the plane the vectors would lie inside, see Equation 3-7. To find the angle, the second plane is the x-y plane with a normal vector along the z-axis. The angle between two normal vectors can be found using the vector identity in Equation 3-8. The simplified Equation 3-9 is used to find the wedge angle under a planar surface approximation.

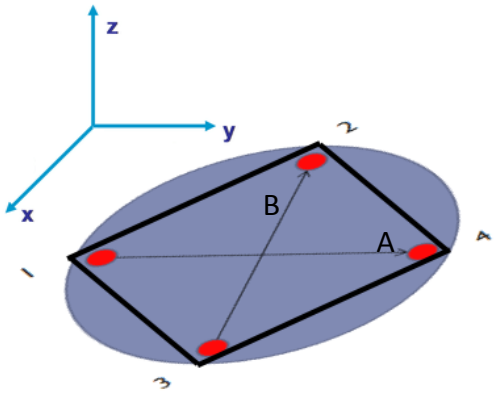

Figure 3.9. Circles indicate OPD sampling points on the wafer indicated by the square. A sample is taken at the center of the wafer for thickness estimation.

$$\vec{A} = \Delta z_1 \hat{z} + d\hat{y} \tag{3-5}$$

$$\vec{B} = \Delta z_2 \hat{z} - d\hat{x} \tag{3-6}$$

$$\vec{A} \times \vec{B} = \vec{C} = d\Delta z_2 \hat{x} - d\Delta z_1 \hat{y} + d^2 \hat{z} \tag{3-7}$$

$$\cos(\theta) = \frac{\vec{C} \cdot \hat{z}}{\|\vec{C}\| \|\vec{z}\|} \tag{3-8}$$

$$\theta = \cos^{-1}\left[\frac{\mathrm{d}}{\sqrt{\mathrm{d}^2 + (\Delta z_1)^2 + (\Delta z_2)^2}}\right] \tag{3-9}$$

3.3.2 Newton's Rings Pattern

The procedure in Equation 3-9 works well when the surfaces are nearly planar, but fails to effectively describe non-uniform wafers. Another technique used in the lab to describe wafers is imaging the Newton's rings of the wafers using a red laser source. This technique can be quantitative or qualitative. It was used qualitatively only, as a means to easily compare one wafer to another based on ring spacing. In Figure 3.10, the wafer on the right is better, due to a sparser Newton's rings pattern. The point at the top of the right wafer where is the Newton's rings pattern stops has the best fringe visibility due to a constant wafer thickness. Quantitatively, at normal incidence, the difference between the OPDs at two similar points on adjacent Newton's rings is the wavelength, see Equation 3-10.

Figure 3.10. Newton's Rings on Circular Wafers.

$$\cos\left(2\pi * \frac{OPD}{\lambda_{red}}\right) = \cos\left(2\pi * \frac{OPD}{\lambda_{red}} + 2\pi\right) = \cos\left(2\pi * \frac{OPD + \lambda_{red}}{\lambda_{red}}\right) \tag{3-10}$$

Similarly, if the angle is changed away from normal incidence(φ), the change in wafer thickness can be calculated by Bragg's Law, see Figure 3.11 and Equation 3-11, by taking two adjacent intensity maxima one wavelength count(m) apart and subtracting them. Finally, the

wedge angle(Ψ) can be calculated using a simple trigonometric identity, shown in Figure 3.12 and Equation 3-12, where L is the separation between the two intensity maxima.

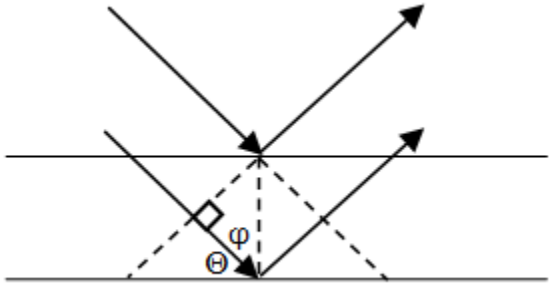

Figure 3.11. The Bragg Law.

$$\lambda = \frac{\lambda_0}{n} \qquad 2dsin\theta = m\lambda = 2dcos\varphi = \frac{m\lambda_0}{n} \qquad \Delta d = \frac{\lambda_0}{2ncos\varphi} \tag{3-11}$$

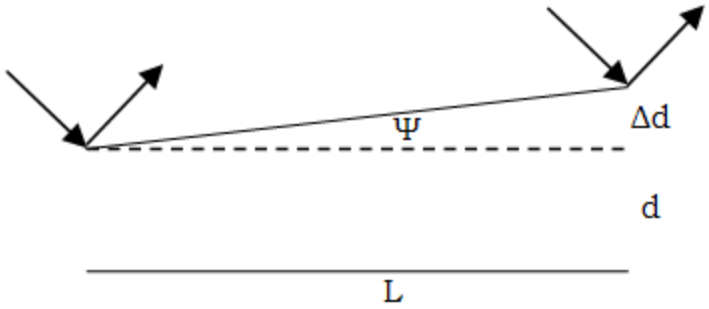

Figure 3.12. Separation between maxima.

$$\Psi = \tan^{-1}\left(\frac{\Delta d}{L}\right) = \tan^{-1}\left(\frac{\lambda_0}{2nLcos\varphi}\right) \tag{3-12}$$

Chapter 4 Sapphire Fiber Solid Cladding

4.1 Introduction to the Cladding Limitation

As discussed in Section 1.1, an optical fiber needs a core and a cladding with appropriate characteristics to guide light under total internal reflection. In a sapphire fiber, the core is high-purity single-crystal sapphire, while the cladding is air. Light propagating through the fiber is guided by the sapphire-to-air interface. A gaseous cladding is vulnerable to contamination from anything that comes in contact with the fiber and contamination leads to optical loss or attenuation. Contamination-induced loss is one of the potential causes of gradual sensor degradation. To prevent this mode of failure, a solid cladding needs to be designed.

A solid cladding for sapphire fiber has several requirements. First, the material must be optically transparent in the working range, 700-1000μm wavelength. Next, the material must have thermal expansion properties similar to sapphire cumulatively in the temperature range of 25-1600^{o}C. The material must also not interact with sapphire to form other material in the temperature range. In addition, the material must have a melting point higher than 1600^{o}C. 1600^{o}C is a bare minimum, but a melting temperature higher than 1800^{o}C is desired. The choice of 1800^{o}C is because sapphire softens at temperatures much lower than its melting point[24]. Finally, the material must be easy to deposit on the surface of the sapphire wafer to a thickness of several microns. At least one wavelength(850nm) thickness is highly desired.

4.2 Material Selection

The materials were identified and evaluated by utilizing many sources including books, journals and company product information posted on the internet. Of all the property requirements stated in Section 4.2.1, the most stringent is the requirement for matching thermal expansion. Thermal expansion characteristics were the starting point and the primary way of identifying new candidate materials. This search was done by manually comparing the CTE values for sapphire against the CTE's of values of other materials in the oxide family. The oxide family was chosen because most oxides are optically transparent and have high melting temperatures. The list of matches further narrowed down by comparing $\Delta L/L_0$ values to

sapphire over all available temperatures, shown in Table 4-1[25]. CTE values describe instantaneous rates of expansion, while $\Delta L/L_0$ values are cumulative. Hence $\Delta L/L_0$ values are more reliable when considering how two materials will expand together from room temperature to 1800°C.

Table 4-1. Materials Identified with $\Delta L/L_0$ Values Similar to Sapphire.

Materials:	
POCO AXM-5Q Graphite	BeO
Dy_2O_3	Er_2O_3
Gd_2O_3	HfO_2
Ho_2O_3	In_2O_3
Lu_2O_3	Pr_2O_3
Sc_2O_3	ThO_2
Tm_2O_3	TiO_2
Yb_2O_3	Y_2O_3

The next step was to find the indexes of refraction and melting points for the materials. The index of refraction has to be lower than that of sapphire as a condition for total internal reflection. Most of the materials were removed from the list, but they are still usable for other purposes in the sensor. The remaining materials with the addition Al_2O_3 are shown in Table and a graph of the thermal expansion $\Delta L/L_0$ values in Figure 4.1.

Table 4-2. Detailed Properties for the Last Round of Candidate Materials.

	Alumina	Beryllia	Praseodymium Oxide
Formula	Al_2O_3	BeO	Pr_2O_3
Melting Point	2072°C	2843°C	2563°C
Refractive Index	1.66	1.7	1.7
$\Delta L/L_0$ Match	Source (Excellent)	Excellent	Excellent
Problem	Can be used only up to 1200°C	Toxic, Gaseous Deposition	1 Å̊ngström/sec deposition rate

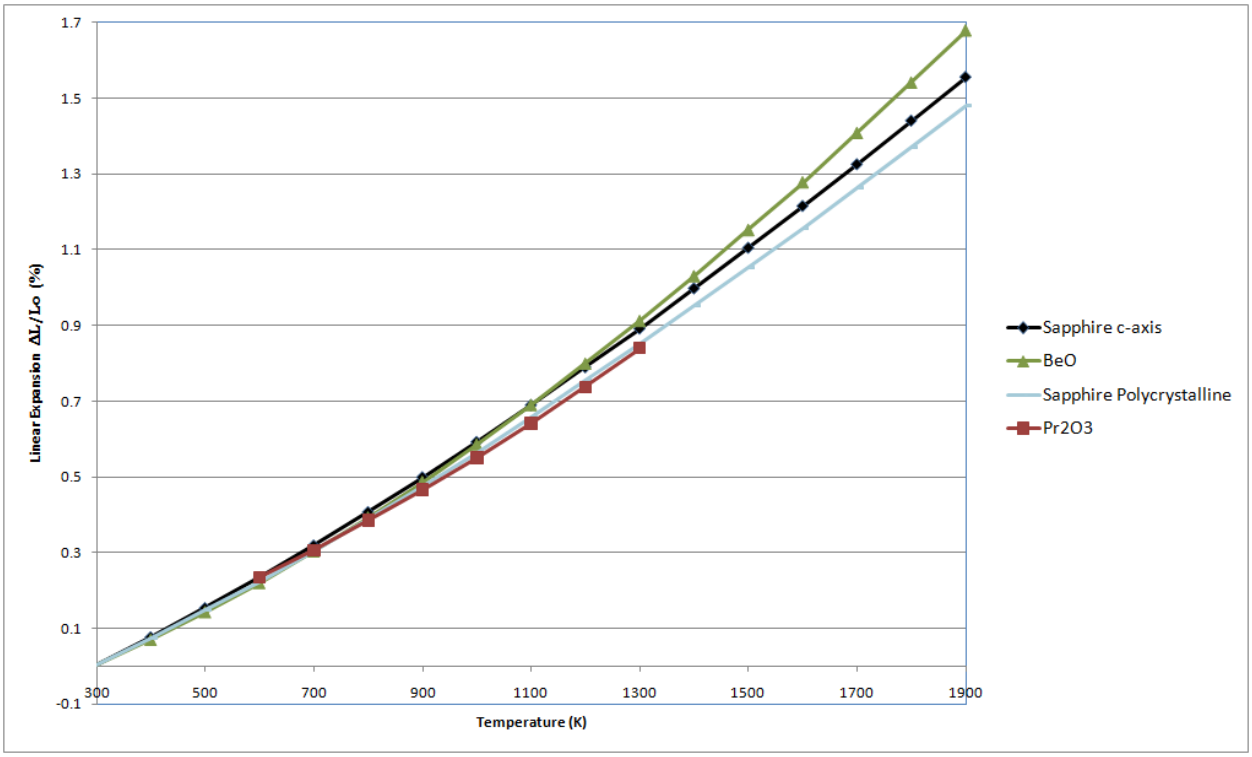

Figure 4.1. Thermal Expansion $\Delta L/L_0$ Values for the Reduced List of Materials.

Berillia and praseodymium oxide are both excellent matches, but because of their other properties, they are not suitable for use. Alumina is the same material as sapphire. The only difference is their structure. At high temperatures, the polymorphous alumina will crystallize and become sapphire, making it indistinguishable from the core. Alumina is only suitable for about the first 10cm of the sapphire fiber, leaving another 40cm unclad. Once again this is not a good solution.

It is quite possible the ideal material does not exist. The additional resources required to use beryllia or praseodymium oxide have made them undesirable but still capable. Clearly, something has to be sacrificed. Trials were done on silica, which is a poor thermal match, but all of the other parameters are a good match. Silica was mainly picked due to availability and cost.

4.3 Deposition of SiO_2 on Sapphire Fiber by PVD

For this study of a solid cladding on sapphire fiber, silica was deposited on two 5cm long pieces and one 15cm long piece of sapphire fiber optically spliced to silica fiber. The deposition

was done by physical vapor deposition using e-beam in a PVD-250 using 99.999% pure 1-5mm size $Si0_2$ pieces in a FABMATE crucible. The fibers suspended vertically with the free sapphire end closest to the crucible and the tip protected from deposition. The deposition yielded a gradient of radially-symmetrical coating thicknesses with the free sapphire end receiving a thicker layer than the spliced end. The fiber was afterwards annealed at 900°C for several hours.

4.4 Classification of Optical Performance

The coating thickness was thickness was approximated using Equation 2-7 from a wideband spectrum taken from a collocated wafer. The bottom of the 5cm sapphire fiber received 476nm coating of silica, while the top received a 453nm thick layer. Both of these values are less than the interrogation wavelength, 850nm, so only partial optical loss protection is expected.

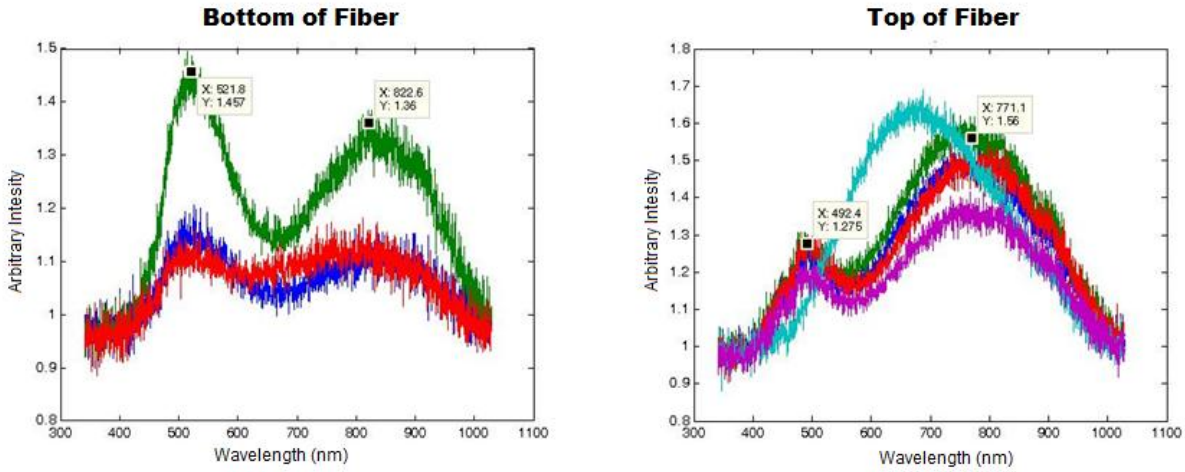

Figure 4.2. Wideband spectrum from the surface of a wafer collocated with the fiber.

4.4 Use of a Calibrated Source of Loss

To quantify the benefits of the silica cladding, it is necessary to be able to apply a repeatable source of optical loss to the surface of the sapphire fiber. After a search for paints, a gold-colored paint containing copper particles was identified. The paint can be applied consistently over 3 cm length of fiber and measured after 5 minutes yielding repeatable loss results as observed in Figure 4.3.

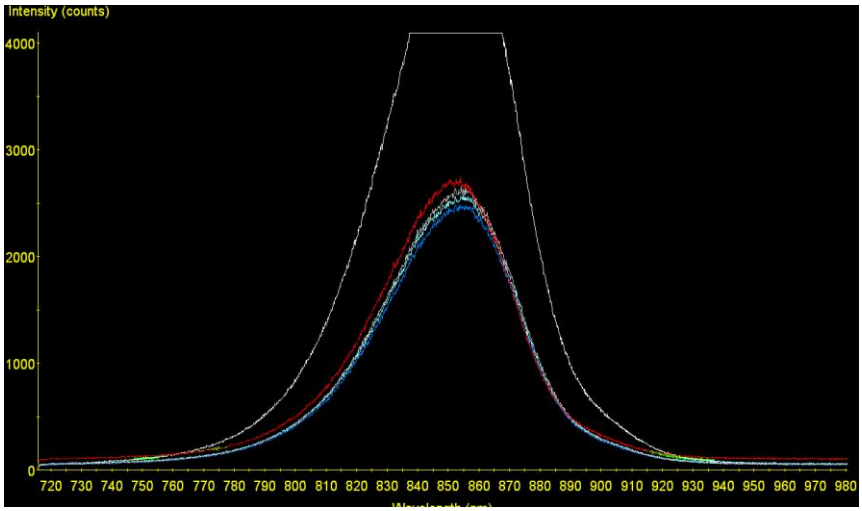

Figure 4.3. Paint Application Repeatibility. The white curve is clean sapphire fiber, while the rest are after application.

In several experiments, the paint was applied to a clean sapphire fiber and the intensity loss was found to be 1.21dB/cm. Next the paint was applied to several silica-clad sapphire fibers. The optical loss from the paint application was found to be 0.17dB/cm. There are also a loss observed to deposition, but it was mostly eliminated by annealing to 900°C. The overall loss due to the deposition of silica on the sapphire fiber is 0.08dB/cm. The total loss from the application of paint on a silica-clad sapphire fiber is 0.25dB/cm, compared to 1.21dB/cm on bare sapphire fiber. That is a nearly 1dB/cm reduction in loss from this paint, as summarized in Table 4-3. There will likely be a similar reduction in loss if other substances are applied as a contaminant to the sapphire fiber.

Table 4-3. Summary of Deposition Contamination-Induced Loss Testing.

Loss Description	**Bare Sapphire Fiber**	**500nm Silica Coating**
Coating-Induced	0dB/cm	0.08dB/cm
Contamination- Induced	1.21dB/cm	0.17dB/cm
Total Loss	1.21dB/cm	0.25dB/cm

One measurement difficulty faced during this study was saturation of the photo detector at the lowest integration time setting. The peak of the signal is not visible, like the

white waveform in Figure 4.3. It became necessary to approximate the location of the peak. A Gaussian distribution was to the not-saturated waveform but the fit was poor. A more elegant solution is to use a not-saturated signal as the fitting model. This resulted in an excellent fit of future signals. An estimation of the saturated peaks using this regression to model approach yielded great results and is visible in Figure 4.4.

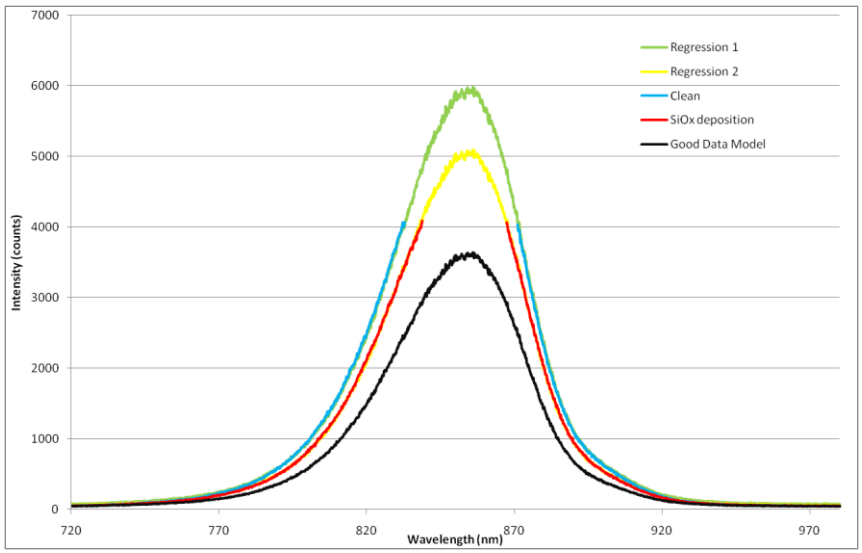

Figure 4.4. Approximation of Saturated Peaks

4.5 Evaluation of the Use of SiO_2 as Cladding

A 1dB/cm loss reduction was observed when a thin silica cladding was applied to sapphire fiber for the particular paint used in this study. Clearly the silica layer is acting as a cladding. If a thicker layer of silica is used, the results will undoubtedly be even better. One important aspect to remember is the poor thermal expansion match between sapphire and silica. This was observed as a fracturing in the silica layer in some fibers as sapphire has a higher CTE than silica. In Figure 4.5, discontinuities in the boundary are visible on the right side of the sapphire fiber after annealing, while the left side is still intact. The optical measurements however prove that this is still a functional design.

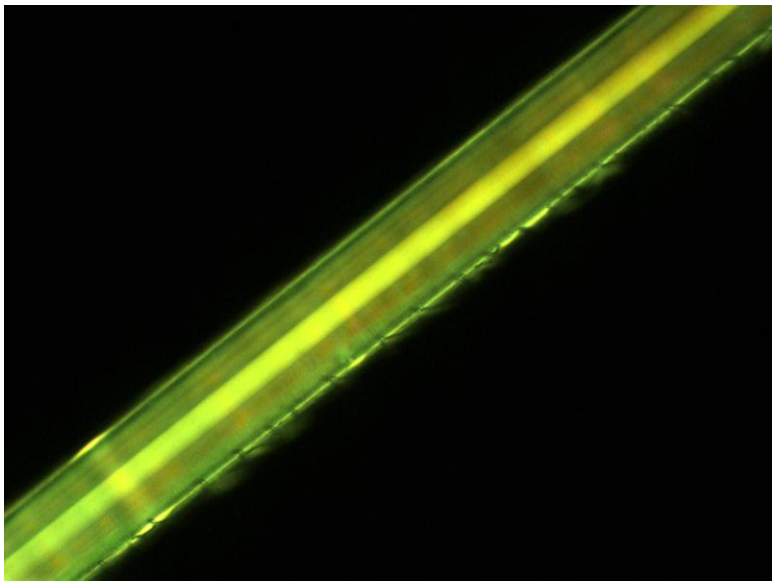

Figure 4.5. Fracturing of the Silica Cladding on Sapphire Fiber

A silica-coated sapphire fiber was inserted into a furnace and raised to progressively higher temperatures. The silica-coating survived at 1000°C, (Figure 4.6 left) without fracturing, but softened and clumped into droplets when heated to a temperature of 1200°C (Figure 4.6 right). These results suggest that the deposited coating may be suitable for operation in the lower-temperature regions of the probe, where contamination was observed to be most severe. The decreased melting point indicates the coating material is not pure and contamination will have to be better controlled in future applications.

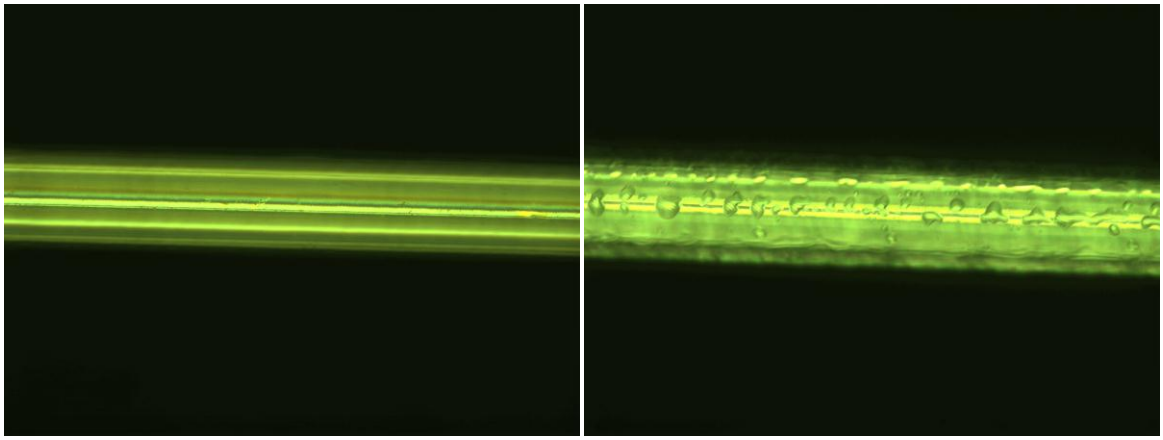

Figure 4.6. Silica-coated sapphire fiber heated to: (left) 1000°C, (right) 1200°C

Chapter 5 Wafer Polishing

5.1 Introduction to Wafer Polishing

The current stock of wafers at the lab is 75μm thick C-plane sapphire wafers supplied by Valley Design. C-plane means all rays propagating in the wafer have ordinary and symmetrical E-field. This is a great simplification in a birefringent material. The best fringe visibility of a near perfect 75μm thick wafer is around 0.1 measured on silica fiber, see Figure 5.1. This is a low fringe visibility that will decrease significantly if measured on sapphire fiber. For the project, a higher fringe visibility in the final assembly is required.

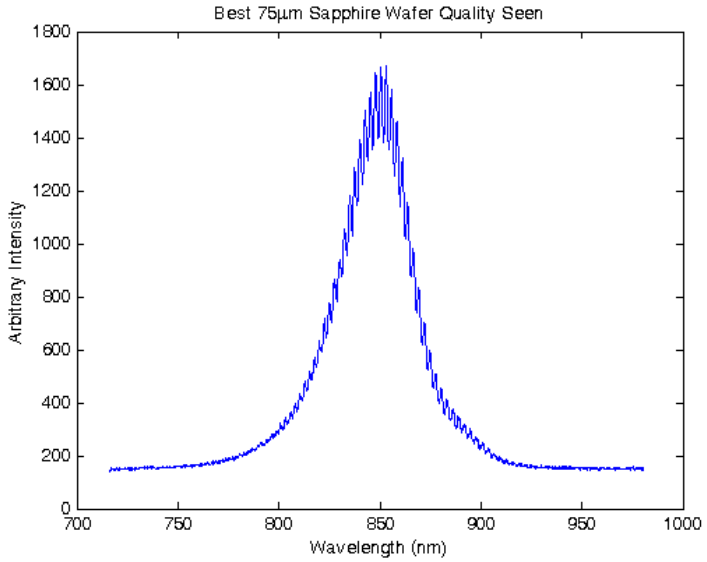

Figure 5.1. Best Fringe Pattern Seen on a 75μm Sapphire Wafer.

A theoretical analysis of low finesse extrinsic Fabry-Perot interferometers was done by Ming Han in 2004[26]. In this study, a comprehensive model for an air gap sensor was developed and confirmed using experimental results. The medium in the cavity is different but the idea is same. Two graphs from the study are shown before. Figure 5.2 shows the dependence of fringe visibility on cavity length and Figure 5.3 shows the dependence of fringe visibility on wedge angle. Clearly, the fringe visibility increases with a decrease in cavity length or a decrease in wedge angle. The wedge angle has a 0.2° tolerance before the fringe visibility is significantly reduced. The wafer thickness however greatly limits fringe visibility. The wafers in stock are 75μm thick, which translates to a 132μm equivalent optical distance in air. Either way,

the maximum fringe visibility that can be obtained theoretically is about 0.2. To increase the fringe visibility, thinner wafers are necessary. In previous years, 50μm wafers were purchased from the same supplier, but are currently unavailable. The availability from Valley Design varies constantly, so thin wafers are not always available and it is necessary to check back from time to time. Many polishing and lapping materials and service providers were contacted; however none could provide ultra-thin optical quality sapphire wafers, with low specified parallelism value. Without a source of the necessary sapphire wafers, many efforts were made to produce them in house.

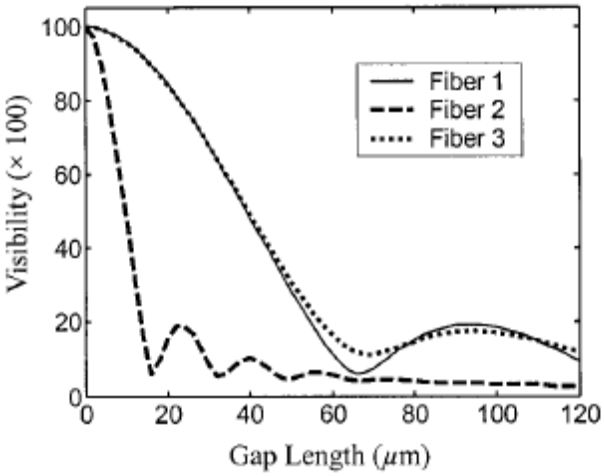

Figure 5.2. Fringe Visibility Dependence on Cavity Length[26].

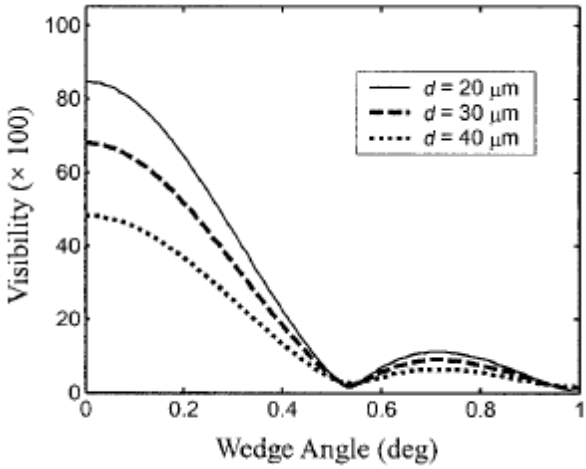

Figure 5.3. Fringe Visibility Dependence on Wedge Angle[26].

5.2 Wafer Polishing Scheme

The polishing was performed using the *Fischione 160 Specimen Grinder* on a standard polishing wheel, shown in Figure 5.4 left. Existing sapphire wafers have some degree wedge angle error. Wedge angle reduction in critical to improved fringe visibility. From Ming's analysis in the previous section, there is a strong correlation between reduced wafer wedge angle, as well as reduced cavity length, and increased fringe visibility. This wedge angle can be reduced by polishing in a plane parallel to the untouched wafer face. The polishing plane is determined by the polishing surface of the grinder. Sources of error during polishing include the parallelism of the grinder polishing plane to the surface of the platen and parallelism of the wafer to the platen surface, see Figure 5.4 right. It is assumed the platen is fixed inside the grinder and the parallelism there does not change, but there is a tolerance in that joint. The following processes seek to minimize wedge angle by increasing parallelism of the wafer to the polishing surface.

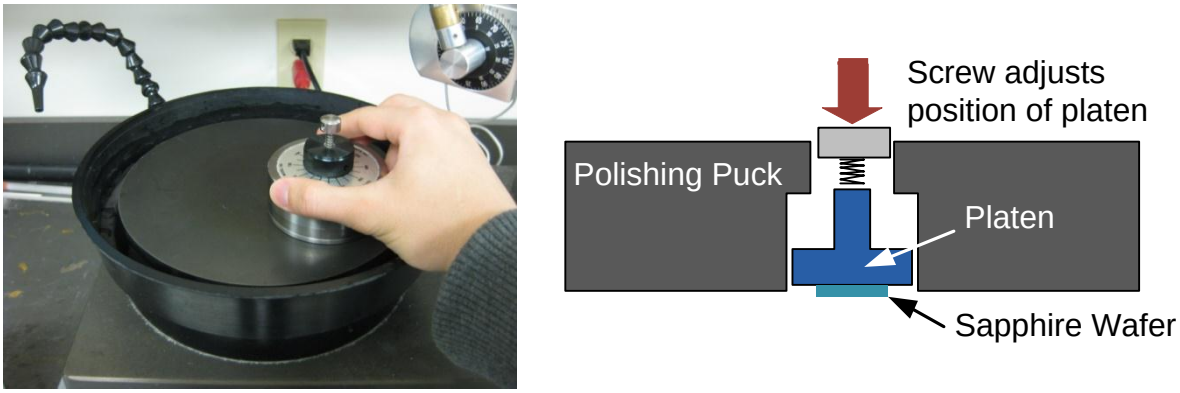

Figure 5.4. Left, *Fischione 160 Specimen Grinder* on the polishing wheel. Right, diagram of the grinder.

The wafers have to be securely mounted to the platen. One adhesive that can be used is Crystalbond 509 from SPI Supplies, shown in Figure 5.5. The simplest mounting procedure and the one recommended by the manufacturer of the grinder is by physical down force on the wafer inside a droplet of adhesive, see Figure 5.6 left-side. First, a drop of Crystalbond is applied to the surface of the platen on a hot plate. Next, the wafer is pushed down with something flat into the droplet so that it lays flat against the platen. The object is retrieved to tend to other wafers, and then platen is cooled down to solidify the adhesive. The goal is to minimize parallelism error between the wafer and the platen.

Figure 5.5. Crystalbond 509[30].

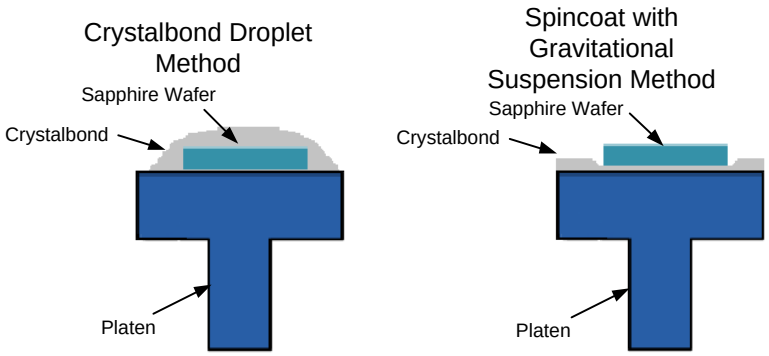

Figure 5.6. Comparison of Wafer Mounting Methods.

5.2 Improvement of Wafer Parallelism

5.3.1 Wafer Mounting to the Grinder Holder

Another way to mount the wafers is by gravitational suspension on a molten spin-coated layer of Crystalbond. First, Crystalbond is spin-coated on a platen using a heat gun to melt it, on the setup shown in Figure 5.7. Next the wafers are overlaid on select parts of the spin-coated layer. The platen is heated on a hot plate so that the wafers adhere to the adhesive by the force of gravity and is then cooled, Figure 5.6 right-side. At this point, more Crystal Bond or super glue is applied over the wafers for protection during polishing. This process was inspired by clean room techniques and seeks to minimize parallelism error between the wafer and the platen. It has shown an improvement in wafer parallelism over the push-down technique. In Figure 5.8 left-side, spin coated Crystalbond after wafer imbedding is visible. The right-side shows a combination of the two methods; where spin-coating was combined with the

push-down technique and an over-coat. The picture was taken after the polishing process was carried out.

Figure 5.7. Spin Coater with custom platen attachment.

Figure 5.8. Left, spin-coated Crystal Bond with 4 1mm diameter wafers imbedded. Right, variety polish product on spin-coated Crystal Bond with Crystal Bond overcoat after polishing.

The fringe visibility and thickness across a single wafer can vary significantly. To further the access the wafer quality, Newton's rings images using visible red light were taken. In combination with the fringe visibility and thickness data across several points on a single wafer, Newton's rings images can paint a very clear picture of the condition of the entire wafer. The Newton's rings patterns of purchased wafers are shown in Figure 5.9, left. The variation in the thickness of the wafers is clearly planar with the left wafer having a smaller wedge angle than the right wafer. Wafers polished using the push down technique described in previous reports, predominantly exhibit a radial ring pattern around the point of contact. Following this discovery, the push down technique was eliminated. The wafers shown on the right-side in Figure 5.9 are

a random selection of wafers polished using the spin-coating technique with the Crystalbond adhesive. Some wafers come out planar, but most have a random variation on the planar pattern. Although the middle wafer pictured seems to have the most obscure Newton's ring pattern, it is by far the best wafer pictured. First, the Newton's rings are spaced further apart suggesting smaller slopes. Second, there are areas where the ring pattern stops, stays constant and then reverses suggesting areas of near perfect wafer parallelism. The ideal Newton's rings pattern of a wafer has no rings at all.

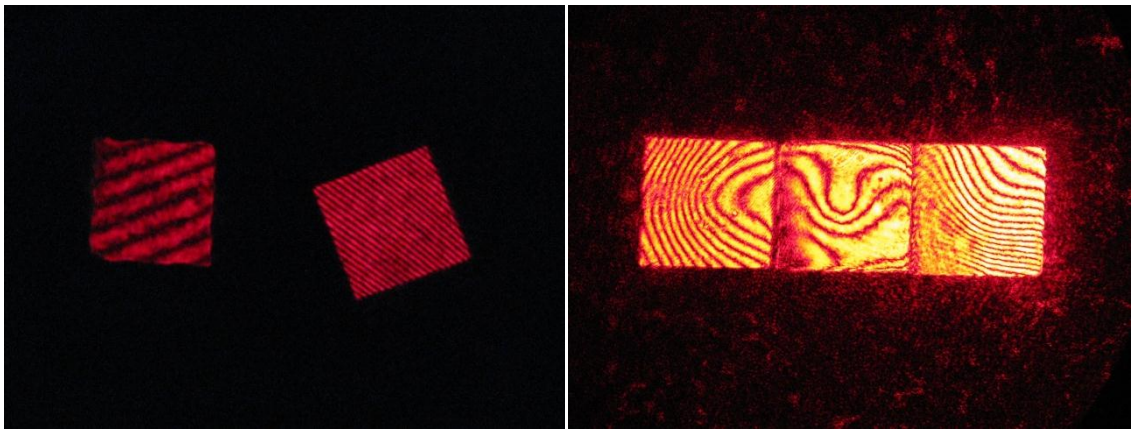

Figure 5.9. Left, professionally polished wafers. Right, in-house polished wafers.

The random nature of these Newton's ring patterns signifies a room for improvement. This probem is attributed to dust contamination of the Crystalbond adhesive and the working area. To mitigate this problem, the Crystalbond is now stored in a sealed environment to protect from dust. Another possibility is spin-coating a new UV-cured adhesive, Norland Optical Adhesive (NOA) 61. This liquid adhesive is much more resistant to contamination, as it is stored in a sealed bottle and dispensed with a built-in dropper. However, this adhesive is difficult to remove and requires submersion in toluene for extended periods. To further decrease the chance of dust contamination, tougher cleanliness practices are performed in a non-clean-room area. This involves thoroughly cleaning the wafers immediately before use, minimizing the movement of clean materials, and minimizing the duration of the wafer mounting process.

5.3.2 Grinder Parallelism

Whether the wedge angle is measured by sampling at multiple points or by Newton's Rings patterns, wedge angles as low as 0.03° and as high as 0.15° are measured. To determine

the grinder's contribution to this angle, methods were devised to quantify the angle between the outer grinder surface and the platen

One method is to clamp the grinder on a tilting platform in the machine shop mill. A micrometer is secured to the drill end. The tilting platform is adjusted until the micrometer reading remains constant when the drill is hand spun over the outer polishing surface of the grinder. This indicates that the drill plane of rotation is parallel to the outer polishing surface of the grinder. Now the micrometer is transitioned to the surface of the platen. As the micrometer is hand spun, the readings are taken repeatedly at 4 equally spaced points, see Figure 5.10. Based on the micrometer offset and the distance between the points using the multiple points method, the angle between the grinder and the platen can be calculated by Equation 3-9.

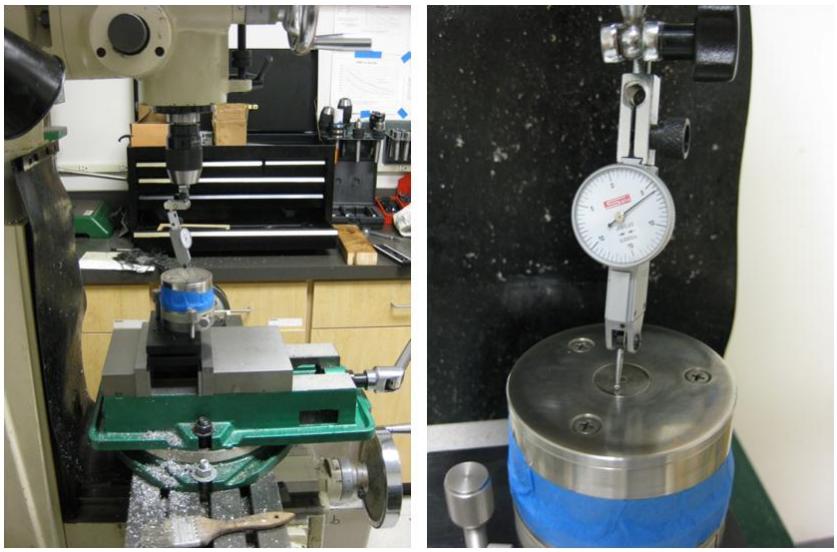

Figure 5.10. Mill Parallelism Measurement Setup.

By conducting the parallelism study, it was determined that the platens are not perfectly parallel to the existing *Fischione 160 Specimen Grinder* polishing surface. To mitigate this error, the grinder was used to polish its own platen until the old platen surface is removed. This process seeks to minimize parallelism error between the grinder polishing surface and the platen surface.

After several platen resurfaces, an unacceptably large tolerance was measured in the mount between the platen and the grinder, allowing the platen to rotate within the grinder more than 1^{o}. Efforts to reduce the tolerance were not as effective as replacing it. The option to

order a new one from Fischione was forgone to save time and to reduce the risk of the new platen also having a large tolerance; it is unknown if the grinder still conforms to Fischione's specifications. Instead, a new tightly-fitting hand-fitted platen made from aluminum was fabricated in the CPT machine shop by a resident expert. The surface of the aluminum platen was polished away to make it parallel to the grinder. Since the advent of the new platen, the wafer polishing wedge angle has become more repeatable and the small.

5.4 Wafer Fracturing Prevention

Wafer thinning is achieved as the last step by polishing more wafer material away to reduce the thickness, see Figure 5.11.

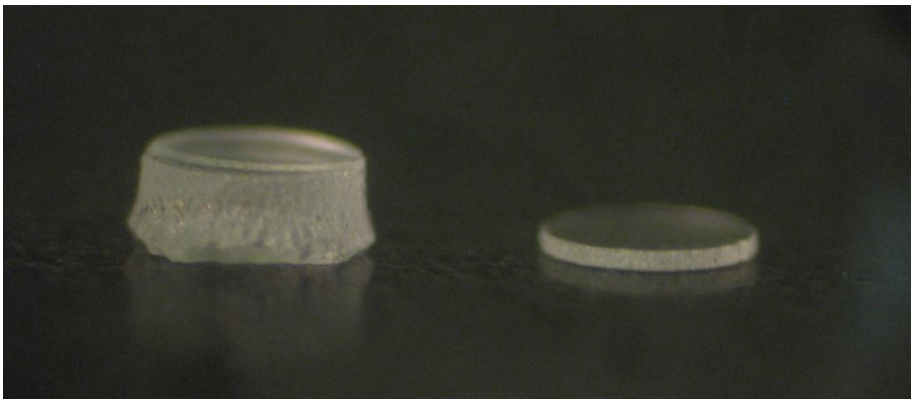

Figure 5.11. Left, 300μm thick wafer after ultrasonic cutting. Right, similar wafer after polishing down to 65μm.

Low yield rates from wafer thinning were problematic due to wafer detachment and wafer fracturing. Wafer detachment is no longer observed as the mounting techniques evolved. Wafer fracturing was greatly reduced by switching to a new wafer thinning process for wafers thinner than 100μm. The previous polishing paper of choice for wafer thinning is 30μm grit diamond paper, allowing good thinning rates and a long polishing paper life. For wafers thinner than 100μm, a 5μm diamond polishing paper grit size is used instead, leading to increased polishing time to thin the wafers and an increased frequency of polishing paper replacement. Only good diamond polishing papers without raised imperfections are used. Additionally, the polishing machine is turned off and the grinder is spun by hand for a more gentle abrasion. It was further necessary to use a material to cover the sides of the wafer when using the spin coat process. Super glue was chosen to for this role as it does not need to be heated up to apply and dissolves in acetone. As a result of these improvements, the majority of wafers do not fracture

and the ones that do only lose small areas and are still usable. This is true even when polishing down to a thickness of 30µm. Thinner wafers have also been achieved; however the wafers are highly likely to fracture. Thin wafers as learned by handling are more brittle.

5.5 Conclusion

Fringe visibility improvements have been achieved by wafer polishing. The wedge angle and Newton's rings patterns are not necessarily better, but the fringe visibility has greatly benefited from a drastic decrease in wafer thickness. The observed fringe visibilities are good enough to meet the demands of the project and are better than those seen in this project at any point in the past. The fringe visibility increased with decreasing wafer thickness as expected, see Figure 5.12 and compare to Figure 5.2.

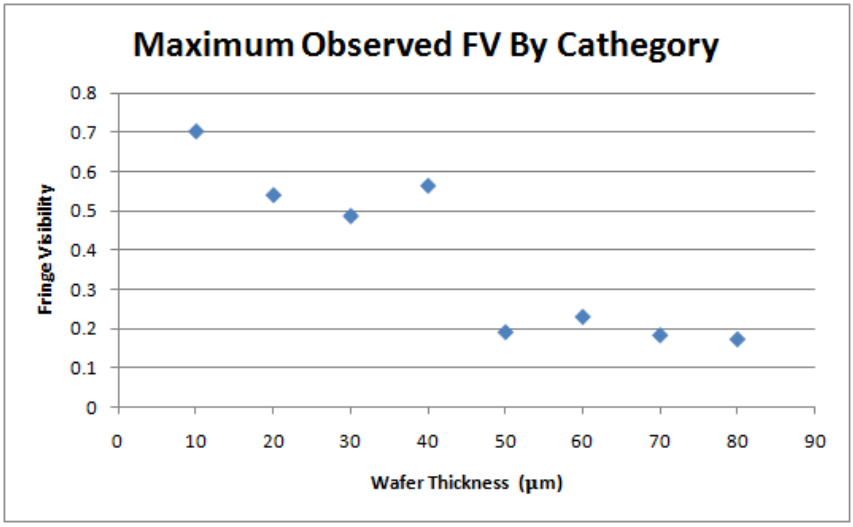

Figure 5.12. Observed maximal fringe visibilities in terms of wafer thickness.

Chapter 6 New Sensor Design

6.1 Overview

In reviewing the results of prior field testing at TECO, one of the potential sensor failure modes has been determined to be an increase in loss in the sapphire fiber during gasifier operation. Post-mortem testing in each of the prior field tests revealed cracking of the outer packaging and deposition of a black contaminant on the optical elements inside the package. This unidentified contaminant appears along the outer surface of the sapphire fiber.

The fibers, however, did not show contamination along their entire length; the 25cm of fiber nearest to the sensor tip appeared to be uncontaminated after deployment in the TECO gasifier. Because the sensor probe extends radially through the gasifier wall, the sensor tip experiences the hottest temperatures, and the environment surrounding the sapphire fiber becomes cooler toward the back of the probe. This means that contamination occurs on the side of the sapphire fiber that is primarily at cooler temperatures.

Based on the uniformity and location of deposition, we hypothesize that the observed phenomenon is a condensation of contaminant gasses in the cooler region of the probe. These gasses likely entered the probe through cracks in the outer package that were caused by differential refractory shift.

6.2 Sensor Head Fabrication

In contrast with the sensor head used in the past, see Figure 2.4, a new design was developed to better protect the optical system, as shown in Figure 6.1. Key improvements include a hermetic seal of the sapphire wafer to preclude detachment or contamination, and a small flexible sapphire tube running the length of the sapphire fiber for structural and contamination protection. This design is based around two concentric tight-tolerance alumina tubes. The inner one serves as an attachment point for the wafer and the sapphire fiber. The outer tube sticks out past the end of the inner tube to provide structural support for the encasement of the sapphire wafer. Other basic supplies used in this sensor not previously mentioned are circular wafers and circular alumina disks. A parallel effort was made by Guo Yu

to cut circles in alumina and sapphire using the Fischione Model 170 Ultrasonic Disk Cutter and diamond particle slurry. That effort has yielded clean-cut circular 1.0mm wafers and alumina disks[18]. The following are processes were used to create a sensor head from the basic parts. Perfect execution of each step in the process of assembling a sensor is critical, because fringe visibility reduction is irreversible. Some steps like the use of a sapphire fiber and the application of adhesives to the sapphire wafer inherently reduce the fringe visibility, but they have been deemed as necessary. It is critical that the fringe visibility is maximally preserved and worst case scenarios are accounted for.

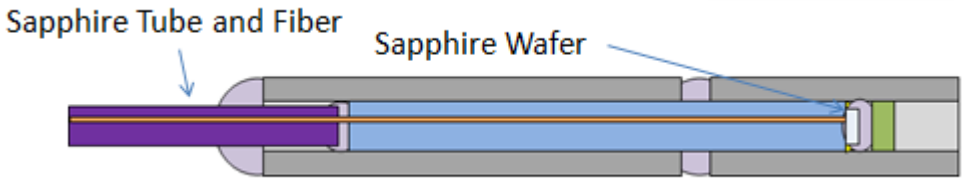

Figure 6.1. New Sensor Design.

6.2.1 Wafer Bonding to the Inner Tube

The alumina adhesive (Resbond 903HP), used to keep this design together, has to be cured in a furnace. It is a thick white liquid that can easily be applied to bond parts. The sapphire wafer bottom optical surface must be kept clean and flush to the inner tube, see Figure 6.2. The top surface of the wafer may be covered in adhesive to fix the wafer in place; however changes in fringe visibility are closely monitored. The alumina adhesive does not offer adhesion until it is cured. The challenge is to keep the wafer stationary until alumina adhesive is cured. Two solutions are discussed below: solgel adhesive and phenyl salicylate wax.

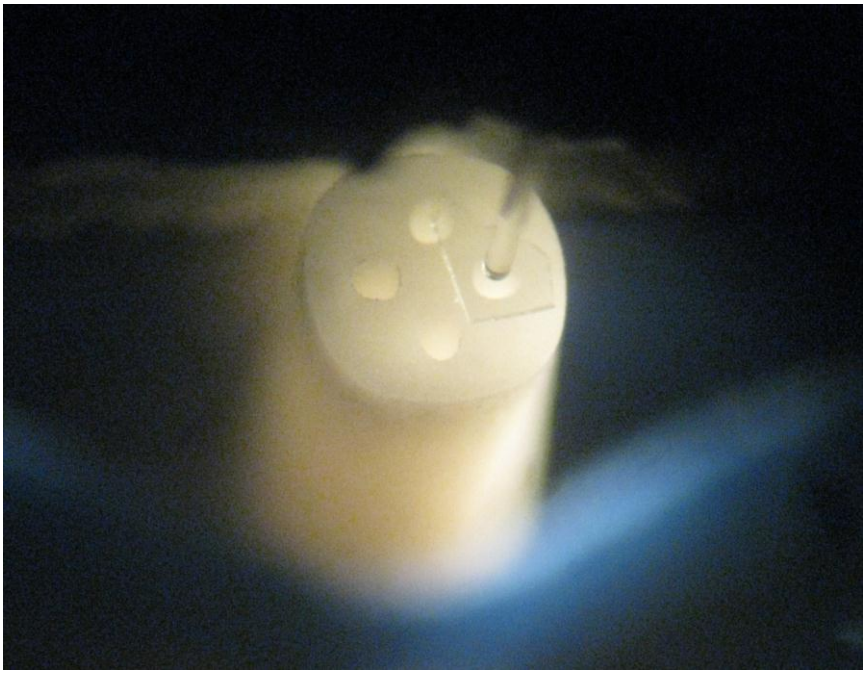

Figure 6.2. Sapphire wafer pinned to the inner tube.

In keeping with previous designs, solgel can be used to quickly bond the sapphire wafer to an alumina tube by the use of a heat gun. Solgel has a very low viscosity and can wet surfaces very quickly. The optical surfaces of the sapphire wafer are not to be covered in solgel, which is very detrimental. For this purpose the wafer is pinned down to the inner tube and a heat gun is used to thicken the solgel as quickly as possible. However, the use of solgel on an object this small is hit or miss in practice. After the solgel is fully cured, alumina adhesive used to bond the inner tube, outer tube and wafer, creating a closed space around the wafer.

An alternative to solgel has been developed. Solgel wetting of the optical surfaces can cut the fringe visibility in half and it is hard to prevent. Instead of trying to prevent the wetting of the sapphire wafer, it is welcomed if the adhesive can be completely removed. Access to the wafer can be obtained through the optical bore of the inner tube, where the sapphire fiber will run. Methods of removal can be any including dissolving, burning, melting and evaporation. The adhesive chosen for this task is phenyl salicylate. It evaporates at around 173°C, which is exceeded by the alumina adhesive curing process. The phenyl salicylate is applied liberally to a pinned wafer and allowed to crystallize. Then a fragment of alumina is attached by the use of more phenyl salicylate or a quick re-melting of the existing by the use of a heat gun, see Figure

6.3. Finally, alumina adhesive is applied at usual and cured. The specifics of this design dictate that the inner tube must be recessed and a circular alumina buffer is firmly placed on top of the alumina adhesive, shown after curing in Figure 6.4.

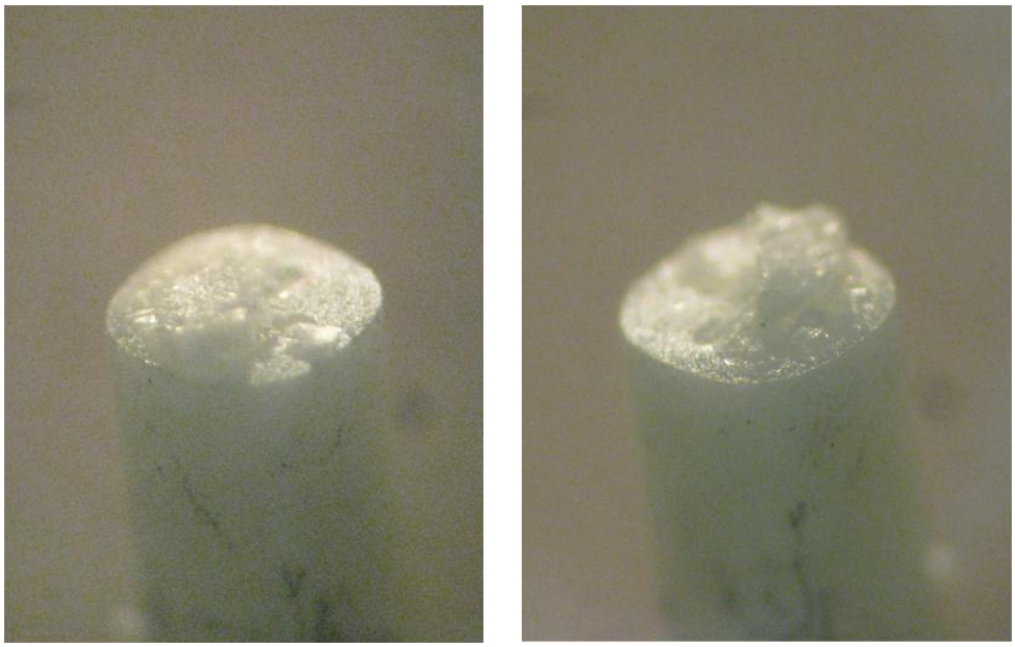

Figure 6.3. Inner tube with a sapphire wafer(left), then alumina buffer(right) attached using phenyl salicylate.

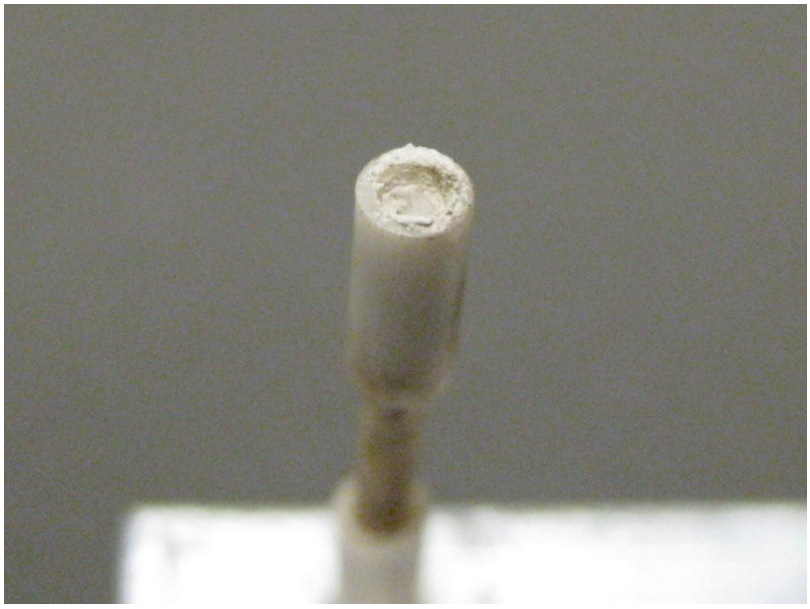

Figure 6.4. Recess in a bonded, but not sealed sensor head.

6.2.2 Laser Sealing

The next step of the process is to hermetically seal the end of the outer alumina tube to serve as the far end of the sensor. To reach the goal of a hermetically sealed sensor, it is necessary to seal one end of the alumina tube. One way of doing this is through thermal fusion, the joining of multiple parts through the application of heat. The advantage here is that thermal fusion uses the existing tubes and can be performed at minimal cost. A disadvantage is the blind inner surface of the seal. Thermal fusion of the tubes leading to similar end results was performed using two different processes.

The first process directly melts the tubes until closed. In this procedure a CO_2 laser with a spherical lens is loosely focused on the end face of the alumina tube. It is exposed to 10-25W until the entire end face melts. After cooling, a domed seal is formed as shown in Figure 6.5. This method causes a lot of damage to the tube, because the laser will continue melting deeper into the tube in a straight line.

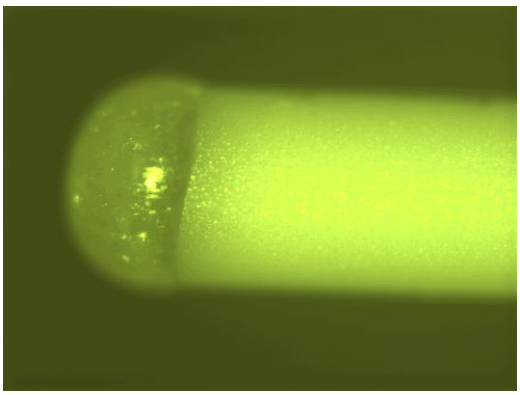

Figure 6.5. CO_2 laser tube melting.

A modification to this process involves melting additional alumina material over the tube end face. The goal here is to reduce the depth of internal damage to the tube. Alumina adsorption powder is piled in a mound and a CO_2 laser is fired into the mound, see Figure 6.6 left-side. As the laser burrows through the powder, it melts the material in its path. The melted material flows down the laser path and accumulates. This process continues until it reaches equilibrium when the accumulated liquid alumina absorbs the laser power. Switching off the laser results in the formation of a solid chunk of alumina (Figure 6.6 center), where increased laser power corresponds to forming an increased nugget size. The nugget is then placed over

the senor recess. A CO_2 laser is fired into the alumina nugget to melt it so it adheres to the tube, see Figure 6.6 right-side. This method is less obtrusive to the tube and should result in a better preservation of the bore.

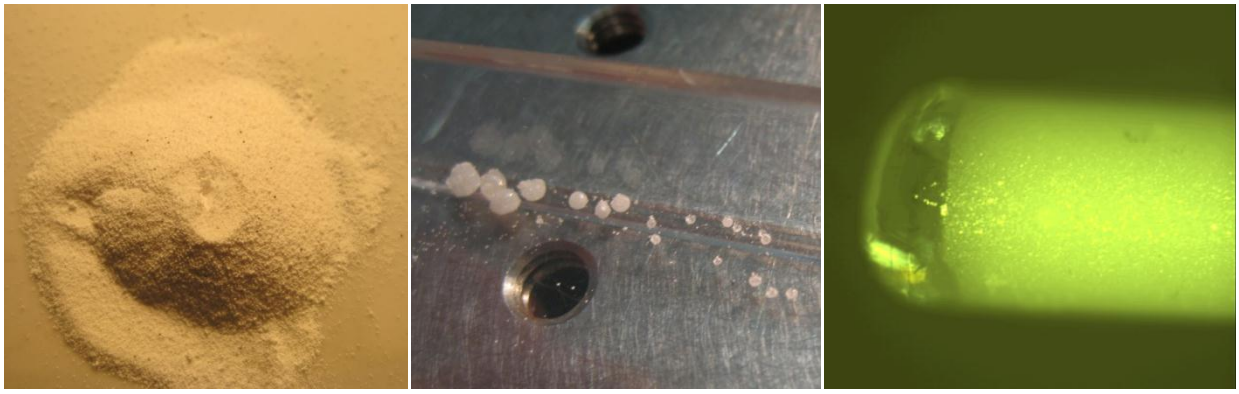

Figure 6.6. Left, alumina adsorption powder with a laser hole. Center, a collection of alumina nuggets. Right, sealed alumina tube.

Questions were raised about the purity of alumina from alumina adsorption, so the previous method was replaced with direct melting of circular alumina disks. A second alumina buffer is adhered to the sensor over the first one using alumina adhesive and cured. To increase the power delivered to the alumina disk, the sensor head was placed inside a pre-heated while lased at 25W with a spherical lens for 10 seconds, see Figure 6.7. The sealed sensor is shown in Figure 6.8. No clear boundary is visible between the alumina disk and outer tube.

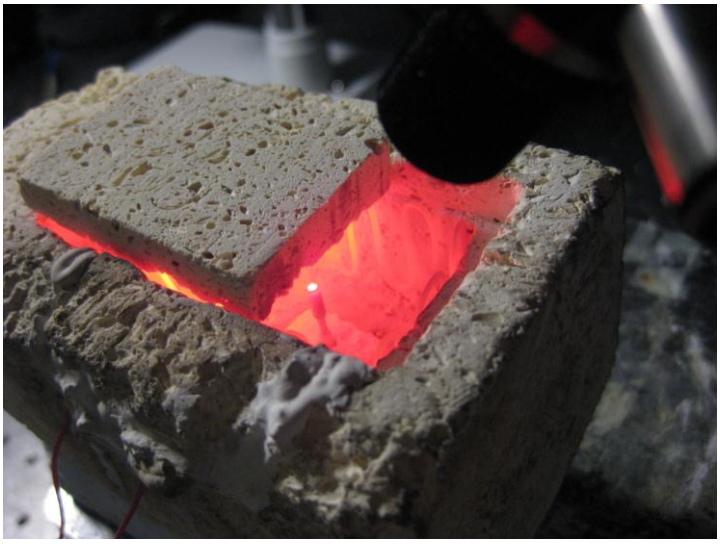

Figure 6.7. Laser Tube Sealing Using Alumina Disks.

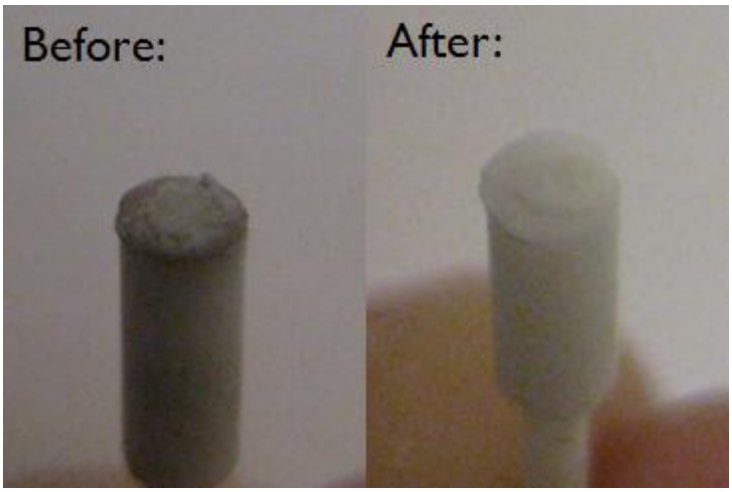

Figure 6.8. Laser Sealing Before and After.

The second alumina disk and alumina adhesive layer are added to increase the distance between the laser melt zone and the sapphire wafer, which can be negatively affected. The complete sealing procedure is shown in Figure 6.9. The sapphire wafer and a small piece of alumina buffer on top are bonded with phenyl salicylate to a polished end-face of the inner tube, from the previous section. From left to right, the outer tube is secured to the inner tube with alumina adhesive, and an alumina buffer pushed inside the tube leaving a recess and packed down. The alumina adhesive is cured. Next, another layer of alumina adhesive and alumina disk are applied to fill up the recess. The alumina adhesive is once again cured. Finally, the sensor is placed inside the pre-heater and the alumina disk at the end is directly melted with a CO_2 laser.

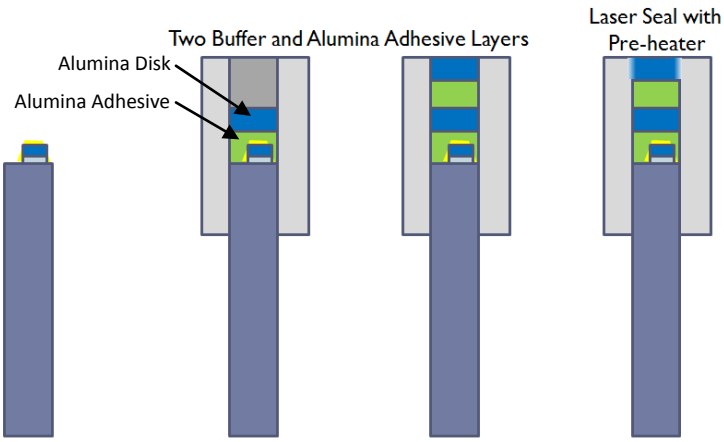

Figure 6.9. Sealing Procedure of the Non-Optical Sensor End.

6.3 Sensor Assembly

Section 6.2 covered the process of creating a sensor head. The product is shown in Figure 6.9 right-side. Once a sensor head is chosen for assembly, an angle-polished sapphire fiber is inserted into the correct bore and bound at the entrance with alumina adhesive. After curing, the sapphire fiber is fixed with respect to the sapphire wafer and the fringe visibility locked. Note, the sapphire fiber was not bound immediately next to the wafer. The sapphire fiber still has the possibility of travel over the area of the bore.

Finally, a second outer tube is slid in over the sapphire fiber to support a sapphire tube, which is partially inserted into the second outer tube. Alumina adhesive is placed between the two outer tubes, between the outer tube and the sapphire tube and at the far end of the sapphire tube which is over silica fiber. After curing the alumina adhesive, the sensor assembly is complete. The next steps are to bundle the complete sensors and built the outer package around them.

6.4 Sensor Performance

The fringe visibility during a sensor fabrication process was measured and recorded at several points, see Table 6-1. The fringe visibility decreased during laser sealing, but it rebounded after the 1600^{o}C annealing. The finished sensor has a 0.23 fringe visibility, but this was not the lowest seen on the sensor head before it was assembled. During the calibration process, the sapphire fiber shifted to a different location with a lower fringe visibility. The decreased fringe visibility at the new location could be because of wafer imperfections or contamination of the wafer optical surfaces. A fringe visibility of 0.10 on the final assembly is still good enough to be used for the blank probe test.

Table 6-1. Fringe Visibility During Sensor Fabrication.

Step in Process	Fringe Visibility
Application of Second Alumina Adhesive Layer	.20
After Laser Sealing	.16

After 1600°C Annealing	.23
After Sensor Fabrication	.23
After Calibration	.10

A temperature calibration curve obtained by heating the sensor to known temperatures and recording the spectrum is shown in Figure 6.10. The signal processing is performed using Cheng Ma's Peak Counting Method using Fabin Shen's Method. The sensor sensitivity is clearly linear. There is also no significant hysteresis in this calibration curve.

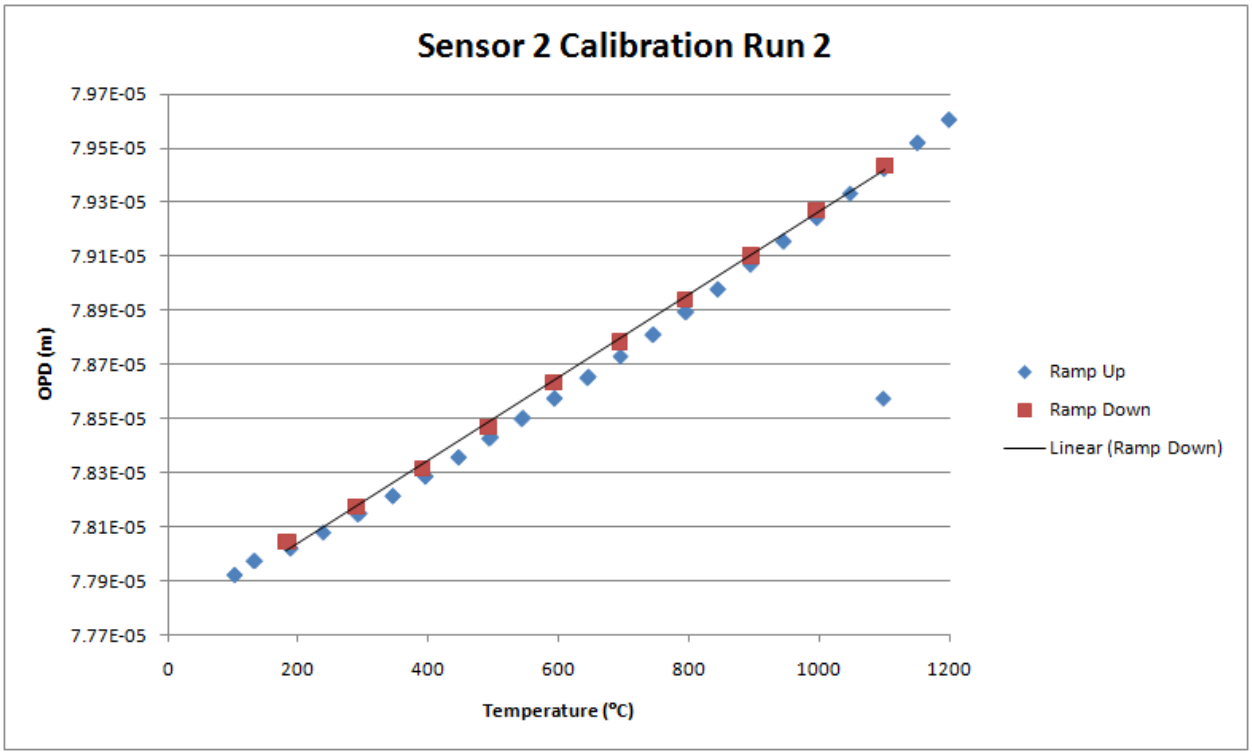

Figure 6.10. Temperature Calibration Curve of a Completed Sensor.

Chapter 7 Summary and Future Work

7.1 Summary

A new sensor design was achieved to address several modes of failure, including sapphire fiber contamination-induced attenuation, Fabry-Perot contamination-induced wafer deterioration and wafer detachment. The sapphire wafer is now securely bonded and hermetically sealed. The sapphire fiber has a possible silica solid-cladding and a sealed sapphire tube to prevent contamination-induced attenuation. The flexible sapphire tube should also provide some physical duress protection for the sapphire fiber. It is hoped the new design will survive longer and more consistently than the previously sensor operating length of 7 months. Field tests are forthcoming and the success of this design will not be known until then.

Design quality will be based on performance inside the coal gasifier during the blank probe and optically monitored tests in 2011 and 2012, respectively.

7.2 Recommendations for Future Work

Although, a new design of the sensor has been completed, there is always room for improvement. The following list is by no means complete, but it seeks to cover currently identified hopes for improvement. It is hoped that future work on this project will address some of these items.

- Spectrometer – The current spectrometer (Ocean Optics 2000) is an older model. Switching the light source and spectrometer is fairly trivial. It would be beneficial to invest in a higher resolution spectrometer, like the Ocean Optics 4000 model.
- Coupler – There is a 3dB loss during any traversal of the coupler. Allocation of a multimode circulator or a 2x1 coupler would result in more optical power delivered.
- Silica/Sapphire Splice Reflection – The most significant reflection in the systems comes from the silica-to-sapphire splice point. This reflection has already been mostly addressed (not part of this thesis). An additional improvement would be the creation of an antireflective coating on the sapphire/silica splice. The main challenge is locating an appropriate optical material that has a refractive index between silica and sapphire's.

- Solid Sapphire Cladding – The silica cladding resulted in a large improvement but it is limited in thickness by the thermal expansion mismatch. A material with a better CTE match can be made thicker to produce a better cladding. One such material is mullite. It is formed by the high temperature annealing of a sapphire and silica combination.
- Thin Film Sensor – The idea of utilizing a thin film instead of the currently used sapphire wafer has been around for several years. This idea has been championed by Jiajun Wang in his dissertation. The realization of this idea has the benefits of the greatly increased fringe visibility and survivability. This approach combined with a thick solid cladding, including the far end of the thin film, would be an extremely robust yet simple combination. A thick film grown on the thin film will not interfere with it in the observed spectral range and resolution combination.
- Currently, the sapphire fiber is allowed to travel within the bore of the inner tube against the wafer, creating vibration modes and differing optical readings. A thin film sensor would automatically solve this problem.

References

[1] Daniel Colladon, “On the reflections of a ray of light inside a parabolic liquid stream”, Comptes Rendus 15, pp. 800-802, 1842

[2] Jeff Hecht, City of Light: The Story of Fiber Optics 1st edition. (Oxford University Press, 1999)

[3] “Solar Lighting - Piped Daylighting Systems”. http://www.fsec.ucf.edu/en/consumer/buildings/basics/windows/solar_lighting/piped.htm. Retrieved 2011-04-07.

[4] Keiser, G. 2003. Optical Fiber Communications. Encyclopedia of Telecommunications

[5] "Thermocouple temperature sensors". Temperatures.com. Retrieved 2011-04-01

[6] R. R. Dils, “High-temperature optical fiber thermometer,” J. Appl. Phys., 54, 1198-1201 (1983)

[7] L. Tong, Y. Shen, L. Ye, and Z. Ding, “A zirconia single-crystal fiber-optic sensor for contact measurement of temperatures above 2000°C,” Meas. Sci. Technol. 10, 607-611 (1999)

[8] J. L. Kenndey, and N. Djeu, “Operation of Yb:YAG fiber-optic temperature sensor up to 1600°C,” Sensors Actuators A 100, 1870191 (2002)

[9] Anbo Wang, George Z. Wang, Kent A. Murphy, and Richard O. Claus, "Birefringence-balanced polarimetric optical fiber sensor for high-temperature measurements," Opt. Lett. **17**, 1391-1393 (1992)

[10] A. Wang, S. Gollapudi, K. A. Murphey, R. G. May, and R. O. Claus, “Sapphire-fiber-based intrinsic Fabry-Perot interferometer,” Opt. Lett., 17, 1021-1223 (1992)

[11] A. Wang, S. Gollapudi, R. G. May, K. A. Murphy, and R. O. Claus, “Advances in sapphire-fiber-based intrinsic interferometric sensors,” Opt. Lett. 17, 1544-1546 (1992)

[12] Kent A. Murphy, Brian R. Fogg, George Z. Wang, Ashish M. Vengsarkar and Richard O. Claus, "Sapphire fiber interferometer for microdisplacement measurements at high temperatures", Proc. SPIE 1588, 117 (1991); doi:10.1117/12.50170

[13] A. Wang, S. Gollapudi, R. G. May, K. A. Murphy, and R. O. Claus, "Sapphire optical fiber-based interferometer for high temperature environmental applications," J. of Smart Materials and Structures, 4, 147-151 (1995)

[14] E. Hecht, Optics, 2nd ed. (Addison-Wesley, Reading, Mass.,1987)

[15] Bing Yu, “Development of Tunable Optical Filters For Interrogation of White-Light Interferometric Sensors,” Virginia Tech Dissertation. (2005)

[16] Ackermann, Gerhard K. “Holography: A Practical Approach,” Wiley-VCH. (2007)

[17] Y. Zhu and A. Wang, "Surface-mount sapphire interferometric temperature sensor," *Applied optics,* vol. 45, pp. 6071-6076, 2006

[18] Guo Yu, “Sapphire-Based Fiber-Optic Sensing for Extreme High Temperatures,” Virginia Tech Thesis. (2011)
[19] Ming Han, “Theoretical and Experimental Study of Low-Finesse Extrinsic Fabry-Perot Interferometric Fiber Optic Sensors,” Virginia Tech Dissertation. (2006)
[20] Lipson, S.G.; Lipson, H.; Tannhauser, D.S. (1995). Optical Physics (3rd ed.). London: Cambridge U.P.. pp. 248. ISBN 0521069262.
[21] Bracewell, R., The Fourier Transform and Its Applications, McGraw-Hill, 1965.
[22] Gary Pickrell, Anbo Wang, “Single-Crystal Sapphire Optical Fiber Sensor Instrumentation: Topical Report,” DOE Award Number: DE-FC26-99FT40685 (2009)
[23] William McC. Siebert (1985). Circuits, signals, and systems. MIT Press. p. 402. ISBN 9780262192293.
[24] Limin Tong, Yonghang Shen, Fangming Chen, and Linhua Ye, "Plastic Bending of Sapphire Fibers for Infrared Sensing and Power-Delivery Applications," Appl. Opt. 39, 494-501 (2000)
[25] National Institute of Standards and Technology, “NIST Structural Ceramics Database (SCD),” http://www.ceramics.nist.gov/srd/scd/Z00665.htm, http://www.ceramics.nist.gov/srd/summary/scdaos.htm.
[26] M. Han and A. Wang, "Exact analysis of low-finesse multimode fiber extrinsic Fabry-Perot interferometers," Applied Optics, vol. 43, pp. 4659-4666, 2004.
[27] Yizheng Zhu, “Miniature Fiber-Optic Sensors for High-Temperature Harsh Environments,” Virginia Tech Dissertation (2007)
[28] MEOS, “OXP-10 Interference,” http://www-2.meos.com/cmd/cms/index.php?id=289.
[29] Wikimedia Commons, “Diffuse Reflection,” http://upload.wikimedia.org/wikipedia/commons/7/79/Diffuse_reflection.PNG.
[30] SPI Supplies, “Material Safety Data Sheet,” http://www.2spi.com/catalog/msds/msds05110.html.
[31] Fabin Shen and Anbo Wang, "Frequency-estimation-based signal-processing algorithm for white-light optical fiber Fabry-Perot interferometers," Appl. Opt. **44**, 5206-5214 (2005)

Appendix A Matlab Code for FOPD

```
%7/26/2010
%Georgi Ivanov
%Jiajun Wang
%Calculates fringe visibility and opd using fft with moderate accuracy.
%Inputs: x and y coordinate row vectors
%Outputs: FV(Fringe Visibility), FSpacing, FOPD,
%FSNR(Signal-to-Noice), Y2(complex fft points)
%nsensors(number of sensors)

function [output] = findFV(datax,datay,nsensors,accurate)
if not((datax(1)==716.04 && datax(end)==980.64) || (datax(1)==717.62 &&
datax(end)==980.91))
   disp('WARNING: Input X is not in the usual range of 716.04nm to 980.64nm');
   %disp('        CORRECTED!');
   %datax=linspace(716.04,980.64,length(datay));
end;
warning off all
nsensors=floor(real(nsensors));
%output=cell(1,nsensors+1);

%%%%%%%%%%%%%%%%%%%%%%%%%%%%%%%%%%%%%%%%%%%%%%%%%%%%%%%%%%%%%%%%%%%%%%%%
%%%%%%%%%%%%%%%%%%%%%
%%%%%          IF NO PEAK FOUND, LOWER THIS NUMBER.              %%%%%
FreqMin=5; %low clipping in the frequency domain to eliminate DC %%%%%%%%%
%%%%%%%%%%%%%%%%%%%%%%%%%%%%%%%%%%%%%%%%%%%%%%%%%%%%%%%%%%%%%%%%%%%%%%%%
%%%%%%%%%%%%%%%%%%%%%

%convert to k space
x1=1./datax;
y1=datay;
x2=linspace(min(x1),max(x1),length(x1));
y2=interp1(x1,y1,x2);

if(accurate)
   stepcount=100;
   steps=1;
   sensize=steps*stepcount;
   FOPD=zeros(1,sensize*nsensors);
   for ii=1:stepcount
      for ij=0:0
         if ij==0
            sy2=y2(ii+1:(end-ii+1));
```

```
        end
        if ij==1
           sy2=y2(ii:(end-ii));
        end
        if ij==2
           sy2=y2(ii:(end-ii+1));
        end
        %fft and abs
        Y2=fft(sy2,length(sy2))/length(sy2);
        Y2abs=abs(Y2);
        %find fringe frequency
        [pks,locs] = findpeaks(Y2abs(FreqMin:floor(end/2)),'sortstr','descend');
        if(isempty(locs))
           disp('WARNING: No Fringes Found(no peak)');
           return
        end
        t=length(sy2)*mean(x2(2:end)-x2(1:end-1)); %total sampling time, 1/t fft spacing, often
3.7701e-004
        %repeat for all sensors
        sensortemp=0; %disregard double peaks and DC random peaks
        for sensor=1:nsensors
           FSNR=pks(sensor+sensortemp)/pks(nsensors+sensortemp+1);
           if(FSNR<1.05 && not(abs(locs(sensor+sensortemp)-locs(nsensors+sensortemp+1))==2))
              while(1)
                 if (locs(sensor+sensortemp)+FreqMin-1)>35
                    disp(strcat('WARNING: Sensor ',sensor,' : No Fringes Found(low SNR)'));
                    FV=0;
                    FSpacing=0;
                    FOPD=0;
                    output{1}=Y2;
                    output{2}=t;
                    output{3}=y2;
                    output{sensor+3}=[FV,FSpacing,FOPD,FSNR];
                    return
                 end
                 if ((Y2abs(locs(sensor+sensortemp)+FreqMin-1)-
Y2abs(locs(sensor+sensortemp)+FreqMin-1-1))/Y2abs(locs(sensor+sensortemp)+FreqMin-
1)<0.05)
                    sensortemp=sensortemp+1;
                 else
                    break
                 end
              end
           end
```

```
            FreqIndex=locs(sensor+sensortemp)+FreqMin-1;
            FreqValue=Y2abs(FreqIndex);
            %approximate fft peak using quadratic function on three points
            quadcoeff=[[(FreqIndex-1)^2,FreqIndex-
1,1];[FreqIndex^2,FreqIndex,1];[(FreqIndex+1)^2,FreqIndex+1,1]]^(-1)*[Y2abs(FreqIndex-
1);Y2abs(FreqIndex);Y2abs(FreqIndex+1)];
            FreqIndexd=-quadcoeff(2,1)/2/quadcoeff(1,1);
            %calculate exact fft peak using fractional fft
            scale=1;
            FreqIndexf=FreqIndexd;
            for decimalplace=1:10
               scale=scale/10;
               low=FreqIndexf-10*scale;
               high=FreqIndexf+10*scale;
               [Y2frac] = continuousfft(sy2,scale,low,high);
               Y2fracabs=abs(Y2frac);
               [fpks,flocs] = findpeaks(Y2fracabs,'sortstr','descend');
               if(isempty(flocs))
                  %disp(strcat('WARNING: Sensor ',num2str(sensor),' : Approximated with only
',num2str(decimalplace),' places'));
                  break
               else
                  if(flocs(1)==1 || flocs(1)==21)
                     disp(strcat('PROGRAMMER ERROR: This should not be possible.
',num2str(flocs(1)),' ',num2str(decimalplace)));
                     FreqIndexf=0;
                     error('here');
                  else
                     FreqIndexf=(flocs(1)-1)*scale+low; %peak approximation, the first location is
"low"
                  end
               end
            end
            %calculate OPD from fft peak location
            FOPD((sensor-1)*sensize+(ii-1)*steps+ij+1)=(FreqIndexf-1)/t; %OPD, point 1 is 0Hz
            if(abs(locs(sensor+sensortemp)-locs(nsensors+sensortemp+1))==2)
               sensortemp=sensortemp+1;
            end
         end
      end
   end
   output{1}=FOPD;
   output{2}=t;
   output{3}=y2;
```

```
   %calculate fringe spacing from fft peak location, only used for Hilbert transform FV function
   FSpacing=length(y2)/(FreqIndexf-1)*mean(datax(2:end)-datax(1:end-1));
   %Fringe Visibility calculation based on approx calubration
   FV=FreqValue/148.6258;
   %save variables
   for sensor=1:nsensors
      output{sensor+3}=[FV,FSpacing,mean(FOPD(((sensor-
1)*sensize+1):(sensor*sensize))),FSNR];
   end
else
   %fft and abs
   Y2=fft(y2,length(y2))/length(y2);
   Y2abs=abs(Y2);
   %find fringe frequency
   [pks,locs] = findpeaks(Y2abs(FreqMin:floor(end/2)),'sortstr','descend');
   if(isempty(locs))
      disp('WARNING: No Fringes Found(no peak)');
      return
   end
   t=length(y2)*mean(x2(2:end)-x2(1:end-1)); %total sampling time, 1/t fft spacing, often
3.7701e-004
   output{1}=Y2;
   output{2}=t;
   output{3}=y2;

   sensortemp=0; %disregard double peaks
   %repeat for all sensors
   for sensor=1:nsensors
      FSNR=pks(sensor+sensortemp)/pks(nsensors+sensortemp+1);
      if(FSNR<1.05 && not(abs(locs(sensor+sensortemp)-locs(nsensors+sensortemp+1))==2))
         while(1)
            if (locs(sensor+sensortemp)+FreqMin-1)>35
               disp(strcat('WARNING: Sensor ',sensor,' : No Fringes Found(low SNR)'));
               FV=0;
               FSpacing=0;
               FOPD=0;
               output{1}=Y2;
               output{2}=t;
               output{3}=y2;
               output{sensor+3}=[FV,FSpacing,FOPD,FSNR];
               return
            end
```

```
            if ((Y2abs(locs(sensor+sensortemp)+FreqMin-1)-
Y2abs(locs(sensor+sensortemp)+FreqMin-1-1))/Y2abs(locs(sensor+sensortemp)+FreqMin-
1)<0.05)
               sensortemp=sensortemp+1;
            else
               break
            end
         end
      end
      FreqIndex=locs(sensor)+FreqMin-1;
      FreqValue=Y2abs(FreqIndex);
      %approximate fft peak using quadratic function on three points
      quadcoeff=[[(FreqIndex-1)^2,FreqIndex-
1,1];[FreqIndex^2,FreqIndex,1];[(FreqIndex+1)^2,FreqIndex+1,1]]^(-1)*[Y2abs(FreqIndex-
1);Y2abs(FreqIndex);Y2abs(FreqIndex+1)];
      FreqIndexd=-quadcoeff(2,1)/2/quadcoeff(1,1);
      %calculate exact fft peak using fractional fft
      scale=1;
      FreqIndexf=FreqIndexd;
      for decimalplace=1:6
         scale=scale/10;
         low=FreqIndexf-10*scale;
         high=FreqIndexf+10*scale;
         [Y2frac] = continuousfft(y2,scale,low,high);
         Y2fracabs=abs(Y2frac);
         [fpks,flocs] = findpeaks(Y2fracabs,'sortstr','descend');
         if(isempty(flocs))
            %disp(strcat('WARNING: Sensor ',num2str(sensor),' : Approximated with only
',num2str(decimalplace),' places'));
            break
         else
            if(flocs(1)==1 || flocs(1)==21)
               disp(strcat('PROGRAMMER ERROR: This should not be possible. ',num2str(flocs(1)),'
',num2str(decimalplace)));
               FreqIndexf=0;
               error('here');
            else
               FreqIndexf=(flocs(1)-1)*scale+low; %peak approximation, the first location is "low"
            end
         end
      end
      %calculate fringe spacing from fft peak location, only used for Hilbert transform FV
function
      FSpacing=length(y2)/(FreqIndexf-1)*mean(datax(2:end)-datax(1:end-1));
```

```
        %calculate OPD from fft peak location
        FOPD=(FreqIndexf-1)/t; %OPD, point 1 is 0Hz
        %Fringe Visibility calculation based on approx calibration
        FV=FreqValue/148.6258;
        %save variables
        output{sensor+3}=[FV,FSpacing,FOPD,FSNR];
        if(abs(locs(sensor+sensortemp)-locs(nsensors+sensortemp+1))==2)
           sensortemp=sensortemp+1;
        end
     end
end
```

Appendix B Matlab Code for Continuous FFT

```
function [Y] = continuousfft(data,scale,low,high)
points=length(data);
if(low<scale)
   low=scale;
end
if(high>points)
   high=points;
end
if(low>=high)
   Y=0;
   disp('bad range');
   return
end
optimizescalar=-2*pi*1i/points;
Y=data*exp(optimizescalar*(0:(points-1))'*((low:scale:high)-1));
```

Appendix C Matlab Code for Fringe Visibility by Michael Fraser

```
function [FC yAh_avg h_fit l_fit] = getfringe(xA, yA, num)
   warning off all
   evals=2500;
   yAh_avg=smooth(yA,num);
   yAh = hilbert(yA-yAh_avg);

   env_h = smooth(sqrt(yAh.*conj(yAh))+yAh_avg,num);
   env_l = smooth(-sqrt(yAh.*conj(yAh))+yAh_avg,num);

   arg_a=fittype('gauss6');
   arg_b=fitoptions('method','NonlinearLeastSquares','Lower',[-Inf -Inf    0 -Inf -Inf    0 -Inf -Inf
0 -Inf -Inf    0 -Inf -Inf    0 -Inf -Inf    0],'MaxFunEvals',evals);

   h_fito = fit(xA,env_h, arg_a, arg_b);
   h_fit = h_fito(xA');

   l_fito = fit(xA,env_l, arg_a, arg_b);
   l_fit = l_fito(xA');

   FC=(max(h_fit)-max(l_fit))/(max(h_fit)+max(l_fit));
end
```

Appendix D Step-by-Step Wafer Polishing Procedure

- Clean-up
  - Clean the platen and the grinder.
  - Zero the platen on the grinder.
- Spin-coat
  - Mount the platen to the spin coater.
  - Clean the outer surface of the Crystalbond stick, if necessary, by dissolving in acetone.
  - Use the heat gun to heat the platen (about one minute).
  - Apply the Crystalbond stick in a circular motion to cover the entire surface of the platen.
  - Spin at 2000RPM for 12 seconds then 3000RPM for 45 seconds, heating until 10 seconds into the high speed cycle.
  - Let it cool. Then remove from the spin coater.
- Set wafers
  - Overlay the measured wafers on the proper side on flat clean areas of the Crystalbond using the vacuum tweezers and a microscope to check orientation.
  - Heat the platen for at least 5 minutes on the hot plate on setting 4 until the Crystalbond is soft and there are visible halos around all of the wafers.
  - Let it cool.
  - Wipe away excess Crystalbond from the edges of the platen using acetone.
  - Measure the depth of the platen on the grinder on a flat surface.
- Overcoat
  - Apply superglue generously to cover all of the wafers, and then wait several hours for it to set.
  - At this point, the wafers should not be visible above the superglue
- Polish
  - Insert the platen into the grinder.
  - Measure the depth of the platen on the grinder on a flat surface.
  - Apply Teflon tape to the platen tucking in the edges. Measure the depth again.
  - Use a 30um grind diamond polishing paper and a continuous spray of water. Rotate the grinder in place continuously when on the polishing wheel. Hold firmly and steadily. To get the polishing paper to adhere to the polishing wheel optimally, spin at maximum RPM for 30 seconds. Polish on the outer surface of the polishing wheel sparingly.
  - Polish away the excess superglue depth at a large step size like 25um at 80-100 RPM.
  - When near the wafers, polish at a step size of about 5-8um at 45RPM or lower.
  - When the desired thickness is reached, switch 9um, 3um and 0.5um grit polishing papers, each for about 5minutes at the same low RPM and without advancing the platen.
- Remove the wafers
  - Remove the platen from the grinder.
  - Insert the platen into pure acetone in a small container until the wafers come lose.
  - Remove the platen from the acetone, and then remove the wafers from the platen keeping track of the top side.

- Optional, clean the wafers individually using an acetone solution in the ultrasound.

❖ Clean-up
- Clean and dry the platen and the grinder.

Appendix E Sensor Assembly Fabrication Procedure Chart